

Received 15 February 2024, accepted 5 March 2024, date of publication 18 March 2024, date of current version 16 April 2024.

Digital Object Identifier 10.1109/ACCESS.2024.3378575

RESEARCH ARTICLE

A Framework for Segmentation and Classification of Blood Cells Using Generative Adversarial Networks

ZAKIR KHAN¹, SYED HAMAD SHIRAZI¹, MUHAMMAD SHAHZAD¹,
ARSLAN MUNIR², (Senior Member, IEEE), ASSAD RASHEED¹,
YONG XIE³, AND SARAH GUL⁴

¹Department of Computer Science and Information Technology, Hazara University Mansehra, Mansehra, Khyber Pakhtunkhwa 21300, Pakistan

²Department of Computer Science, Kansas State University, Manhattan, KS 66506, USA

³Department of Computer Application and Technology, Qinghai University, Xining, Qinghai 810016, China

⁴Biological Sciences, International Islamic University Islamabad, Islamabad 44000, Pakistan

Corresponding author: Syed Hamad Shirazi (syedhamad@hu.edu.pk)

This work was supported by the Higher Education Commission (HEC) Pakistan through the National Research Program for Universities (NRPU) under Project 16017.

ABSTRACT Blood smear analysis is often used to diagnose diseases like malaria, Anemia, Leukemia, etc. Morphological changes, such as size, shapes, and color, are receiving much attention in pathological analysis. Existing methods for detecting, diagnosing and analyzing blood smears cannot quantify overlapped, irregular boundaries and complex structures. This work proposes and evaluates a framework that utilizes Generative adversarial networks (GANs) for the segmentation and classification of blood elements, that is, white blood cells (WBCs), red blood cells (RBCs), and platelets (PLTs) simultaneously. The Generator of the network determines the mapping from microscopic images of blood cells to a confidence map. This mapping stipulates the probabilities of the pixel of the microscopic blood cell images with respect to ground truth. The Discriminator of the network is essential to castigate the mismatch between the microscopic blood cells images and confidence map. Additionally, adversarial learning enables the Generator to generate a qualitative confidence map that is converted into segmented images. We have calculated minimum, maximum, and average losses to judge the performance of the proposed model. We measure structural similarity, peak signal-to-noise ratio, pixel classification error, and finally, classified cells. The proposed framework can analyze all the blood cell elements simultaneously. The proposed framework shows a significant improvement in the segmentation and classification of blood cell elements compared to state-of-the-art techniques. During the training process, generator total loss reduces by 12.18%, 5.39%, and 3.62% for RBCs, WBCs, and PLTs, respectively. Our results demonstrate that the proposed framework outperforms existing state-of-the-art techniques, achieving the highest pixel correctly classified (PCC) ratio for the segmentation of blood cells as 99.8%, 93.4%, and 99.9% for WBCs, RBCs, and PLTs, respectively. Our framework attains 95.45% and 88.89% classification accuracy for WBCs on ALL-IDB-I and ALL-IDB-II datasets. The dataset used for this study can be found at <https://drive.google.com/drive/folders/1F7kZ1SRWUD9R6aHLMkj3wsjcHnvlGuwP?usp=sharing>

INDEX TERMS Segmentation, classification, convolutional neural network, generator, discriminator, generative adversarial network, healthcare, medical imaging.

The associate editor coordinating the review of this manuscript and approving it for publication was Amin Zehtabian^{id}.

I. INTRODUCTION

Accurate and efficient segmentation of blood smear has a pivotal role for the diagnosis of several blood related diseases like Anemia, malaria, Leukemia and many other [1].

However, blood smear segmentation is difficult because of the high variability and complexity of blood cell shapes, sizes, and appearances. Moreover, obtaining a large and diverse dataset of annotated blood cell images is costly and time-consuming. Accurate blood smear segmentation is crucial for diagnosing diseases because it can provide valuable information about the health status and condition of a patient. For example, blood image segmentation can help to: 1) Measure the blood cell count and ratio, 2) Identify the blood cell morphology and deformities and 3) Classify the blood cell type and subtype. An abnormal cell condition can be pointed out with the analysis of the blood cells' shape, size, morphological, and statistical features. The diagnostic process of blood-related disease mainly relies on the pathological characterization and identification of blood samples [2]. Generally, white blood cells (WBCs) can be classified into two main categories, that is, healthy and unhealthy. There are five pathological classifications of WBCs based on the shape and texture of the cell.

Precise cell detection and classification are still challenging in medical image processing due to cell structure variations, inconsistent and insufficient information on staining and heterogeneous illumination variations [3]. Cell detection and classification are essential steps for blood smear segmentation, that help us to identify and separate different types of blood cells from microscopic images. Pathologists face several challenges during cell detection and classification. Some of these challenges are given below:-

- **High variability and complexity of blood cells:** Blood cells have different shapes, sizes, and appearances depending upon cell type, condition, and morphological structure. For example, red blood cells (RBCs) can be normal, abnormal, or infected, white blood cells (WBCs) can be classified into five subtypes with different morphologies, and platelets can be combined or dispersed.
- **Limited and imbalanced data:** Obtaining a large and diverse dataset of annotated blood cell images is costly and time-consuming. Manual annotation requires expert knowledge and skills that can lead to human errors and inconsistencies. Furthermore, some types of blood cells are underrepresented in the dataset, which can lead to data imbalance and biasness.
- **Domain adaptation:** Blood cell images can vary significantly depending on the imaging modality, device, setting, and protocol used to acquire the images from blood smear slides. For example, different microscopes can have different magnifications, resolutions, contrasts, and noises. These variations can affect the quality and characteristics of the images and make it challenging to apply detection and classification models across different domains.

In addressing the complexities of blood cell segmentation and classification, the use of generative adversarial network (GAN) models is beneficial. GANs excel in pixel-level analy-

sis, generating synthetic images that capture the morphology of blood cells. By justifying data shortage and imbalance, they enhance model robustness.

Generative adversarial networks (GANs) are a type of neural network that can generate realistic images from random noise. A GAN is a generative model that works efficiently against adversarial problems. GAN consists of two components: a Generator and a Discriminator. The generator tries to produce images that look real, while the discriminator tries to distinguish between real and fake or generated images. The two components compete with each other in a minimax game, where the generator aims to fool the discriminator, and the discriminator aims to classify the images correctly as real or fake. Conditional GAN (cGAN) is an extension of GAN that can generate images based on some condition that is given as additional information to the model, such as class labels, text descriptions, or other images. cGAN uses the same architecture as GAN, but both the generator and the discriminator receive conditional information as input. In this way, the generator can produce images that match the given condition, and the discriminator can also use the condition to evaluate the images. The segmentation and classification of blood cells have several challenges, such as limited training data, complex and diverse cell shapes, and imbalanced classes of training data. To overcome these challenges, we need data augmentation, data adaptation, and learning of complex cell shape, the cGAN is suitable. cGANs are relevant to blood cell segmentation because it can help to identify and separate different types of blood cells, such as RBCs, WBCs, and platelets. Segmentation and classification are important for diagnosing various blood disorders, such as anemia, leukemia, and malaria. cGANs can help to improve blood cell segmentation by generating synthetic images that can augment the existing data or transfer knowledge from other domains. For example, cGANs can be used to generate images of blood cells with specific labels or attributes, such as cell type or cell count.

GAN-based approaches can help to improve blood cell segmentation by: **Increasing the size and diversity of the data:** GAN can generate synthetic images of blood cells with different morphologies and conditions, such as normal, abnormal, or infected cells. These synthetic images can be used to augment the existing data and increase its size and diversity. This can help to reduce overfitting and improve the generalization of segmentation models. **Balancing the data distribution:** GANs can generate synthetic images of blood cells with specific labels or attributes, such as cell type, cell count, etc. These artificial images can be used to balance the data distribution and overcome the problem of data imbalance, which ultimately improves the performance and robustness of segmentation models.

The key contributions of this research are highlighted below.

- Based on conditional GAN (cGAN): The neural network used for generating new data based on a set of inputs, we propose RWP-GAN, that is, a GAN for

segmentation of red blood cells (RBCs), white blood cells (WBCs), and platelets (PLTs) in whole-slide as well as single-cell images. We train RWP-GAN with spectral normalization and gradient penalty for segmentation. We have used adversarial learning for higher order spatial consistency and post-processing. The problem is considered as a regression problem where the loss function is learned during training.

- Statistical analysis of the shape, size, and color-texture features of whole-slide and unicellular images using a single generalized model.
- Due to the unavailability of labeled blood cell segmented data, we have developed an extended version of two databases, ALL-IDB-I and ALL-IDB-II by creating manually segmented images for each type of cell. The extended databases contain annotated synthetic blood cell images. Both extended versions of databases are made open source for non-commercial use only.

The remainder of the paper is organized as follows: Section II describes the architecture of the proposed framework, databases description, and training details. The section further elaborates on the working pipeline for segmentation and classification. Results and discussions are presented in Section III. Finally, conclusions are drawn in Section IV.

II. RELATED WORK

The application of Generative Adversarial Networks (GANs) in medical imaging has seen a penetration in recent years, especially in the domain of blood cell segmentation and classification. These studies highlight the evolving of GAN applications in blood cell imaging, pointing to a future where GANs play a central role in advancing diagnostic accuracy and efficiency.

Pixel-level classification and recognition of microscopic blood cell images are helpful for extracting meaningful information and identification of blood constituents [4]. Recently, most of the segmentation and classification techniques have been proposed [5], [6], [7], [34] using color spaces like LAB (Lightness, A Channel, B Channel), RGB (Red, Green, Blue), HIS (Hue, Saturation, Intensity), etc., for the separation of blood constituents. Blood cell segmentation based on morphological features like shape, size, color, geometry and texture is used [8], [9], [10], [11]. These techniques focused on single microscopic blood cell analysis. In [4], the Muhammad Shahzad et. al have performed segmentation of blood cells from whole slide images. However, only one type of blood element can be segmented and classified from the unicellular image. A wide range of techniques like convolutional neural networks (CNNs) [2], [12], [13], clustering [7], semantic segmentation [14], [15], [16], [17], and marker-controlled watershed algorithms [9], [18] have been used to achieve different ranges of results and performances. In [44], the authors provide a detailed review of the GAN application in the medical image segmentation domain with respect to the GAN-based models, augmentation

methods, performance matrices, dataset, implementation, and loss function. Using non-invasive ultrasound images, [45] accurately segment breast tumors with the help of a probability map generative network (PMG). The author used the Dice Similarity Coefficient (DSC) approach to evaluate the proposed model. In [46], the authors use a GAN network to recognize abnormal blood cells using normalized digital color staining. The network comprises two GANs network: GAN_1 work with the PIX2PIX technique to transform the original image into an adoptive greyscale, while GAN_2 transforms it into a normalized RGB image. The author [47] developed a Synthetic Cell GAN (SCG) that comprises two sequential GAN networks. This network helps to automatic identification of WBC by generating synthetic images.

In [50] and [51], the authors carry out a comprehensive review of GAN applications in medical image segmentation, focusing on the diversity of GAN-based models, augmentation methods, performance metrics, dataset implementation, and loss function considerations. Study performed by [52] and [67], non-invasive ultrasound images were used to segment breast tumors effectively using a digital mammogram while [53] used supervised U-net for liver tumor segmentation effectively. The methodology involves generating a probability map that accurately depicts the presence of tumors, evaluated using the Dice Similarity Coefficient. The use of Deep Convolutional Generative Adversarial Networks (DCGAN) to augment image samples was highlighted by [54]. This was further enhanced by matrix transformations and combined with ResNet for WBCs classification. Morphological operations and image digitization followed this [56] for blood cell segmentation. Reference [4] introduced a semantic segmentation approach for WBCs, RBC and platelets that incorporated pixel-level labeling and color space conversion. In [58], the authors presented a leukemia prediction method using the HoG descriptor and LR based on the ALL-IDB dataset. The SURF feature, combined with GA, achieved a notable 92% accuracy in feature extraction [61]. Other notable feature detectors include SIFT [62], FAST [63], and CenSurE [64]. The fusion of hand-crafted features has been suggested to enhance performance [65]. Traditional methods of blood cell analysis, while accurate, are labor-intensive and have limitations in robustness. The rise of deep learning and convolutional neural networks has paved the way for automatic feature extraction, with models like AlexNet, GoogleNet [66], ResNet, and VGG-16 being prominent examples. The SESSA algorithm then refines the extracted features. Combining DC-GAN with ResNet for Blood Cell Image Classification [54] focuses on the significance of WBCs in the human immune system and their role in clinical diagnosis and therapy. This paper introduces a novel framework for blood cell image classification that combines a Deep Convolutional Generative Adversarial Network (DC-GAN) with a Residual Neural Network (ResNet). The introduced loss function enhances the discriminative power of deeply learned features. Experimental results indicate that the model achieves a classification

accuracy of 91.7% for WBC images. The research carried out by [68] focuses on the segmentation and classification of white blood cells (WBCs) to diagnose leukemia, a prevalent blood cancer caused by an overproduction of immature WBCs. The proposed technique involves two main stages: 1) Preprocessing-based classification and 2) Segmentation. In preprocessing, GAN is used for the generation of synthetic images, and then color is used for normalization. Pretrained models, i.e., DarkNet-53 and ShuffleNet, were used for the extraction of deep features from each blood smear image. The proposed method achieved high accuracy in classification and segmentation, outperforming existing research works. The above literature reflect the broad spectrum of GAN applications in medical imaging. While our study focuses on the segmentation and classification of blood cells using GAN. The recent advancements provide a context of how GANs are being modified to address specific challenges in medical imaging. While the proposed research contributes to this developing field by demonstrating the effectiveness of GANs in handling simultaneous segmentation and classification of different blood cell types.

In [48], the author addresses the challenge of automating the classification of cells from bone marrow used for leukaemia diagnosis. The authors propose a three-stage approach involving a novel C-WGAN-GP to generate realistic synthetic cell images and a sequential CNN for classification. The models achieve a 96.98% accuracy using synthetic data and a 14.52 ± 0.10 inception score. A novel approach was developed by [49] to the automatic generation of masks. This approach adds masks on four distinct channels, ensuring no overlap within the same channel at a precisely 2-pixel distance. The above literature reflect the broad spectrum of GAN applications in medical imaging. While our study focuses on the segmentation and classification of blood cells using GAN. The recent advancements provide a context of how GANs are being modified to address specific challenges in medical imaging. While the proposed research contributes to this developing field by demonstrating the effectiveness of GANs in handling simultaneous segmentation and classification of different blood cell types. However, above techniques fail to deal with complex biological appearances, noisy samples, and heterogeneous illumination variations without additional tedious processing steps. In this paper, adversarial learning is used to segment blood cells (WBCs, RBCs and platelets) to overcome the problem mentioned above. The proposed framework targets whole-slide images (WSIs) and single-cell images for segmentation. In 2014, Ian Goodfellow introduced generative adversarial networks (GANs) [19]. Since then, GANs have been used in various medical imaging applications like reconstruction [20], [21], segmentation [22], [23], [24], detection [25], [26], translation [27] and co-adoption [28].

III. PROPOSED FRAMEWORK

This section describes the working mechanism of the proposed framework named RWP-GAN, shown in Fig-

ure 1. The primary aim behind the RWP-GAN model is precise and proficient segmentation of blood cell elements. The framework is divided into two components: Generator (G) and Discriminator (D). Generator (G) shows analogy with counterfeit's team whose aim is to generate fake currency and put it on the market for utilization. In contrast, Discriminator (D) shows analogy with detective personnel whose aim is to detect the forged currency in the market. A GAN consists of special training algorithms that train both (G) and (D) component adversarial with dropout and back-propagation [28].

One of the key challenges in blood cell segmentation is identifying each class cell boundary. Typical CNN-based approaches depend on the minimization of the pixel-to-pixel loss. Although single pixel loss is negligible for the overall loss, it contributes much to segmenting multiple blood cells compared to single blood cells. The GAN-based segmentation models can learn from the loss function that delineates the difference between manually segmented and generated images. This has been investigated comprehensively in image-to-image translation models [27], [29]. Such methods can compute subtle variation in a range of higher-order statistics (HOS) between manually segmented ground-truth and predicted blood cells segmented images. The GANs can compute a loss based on the decision about the output image as a fake/machine-segmented or real/manually-segmented. The iterative training of the GAN-based segmentation network enables it to reduce this loss. In RWP-GAN, instead of dealing with each pixel independently conditionally from all other pixels, it considers a larger receptive field and learns a structured context-aware loss. The RWP-GAN learns a mapping relation for blood cell segmentation that can compare blood cell images to their target segmented image. For the training of the proposed model with paired data for segmentation, the objective of RWP-GAN is to reduce per pixel loss L_1 as well as an adversarial loss $L_{RWP-GAN}$ to castigate the segmentation errors and joint configuration of pixels. In RWP-GAN, the adversarial loss is similar to cycle GAN loss [27], in which the Discriminator and Generator play a min-max game to minimize the errors and maximize the objective. Hence, the objective of RWP-GAN can be evaluated by comparing the cross-entropy between the real and generated distributions and expressed as:

$$\begin{aligned} \min_G \max_D (G, D) \\ = E_{xy}[\log(D(x, y))] + E_{xz}[\log(1 - D(x, G(x, z)))] \quad (1) \end{aligned}$$

In Equation 1, $D(x, y)$ indicates the probability of mapping between the input image x and the target image y . E_{xy} is expected to map between real input and manually segmented target image y . $G(x, z)$ is the output of the Generator on a given input x and the randomized noise z . However, $D(x, G(x, z))$ represents the probability that the Generator's segmented images $G(x, z)$ are equivalent to segmented ground-truth images. E_{xz} is the expected mapping relation

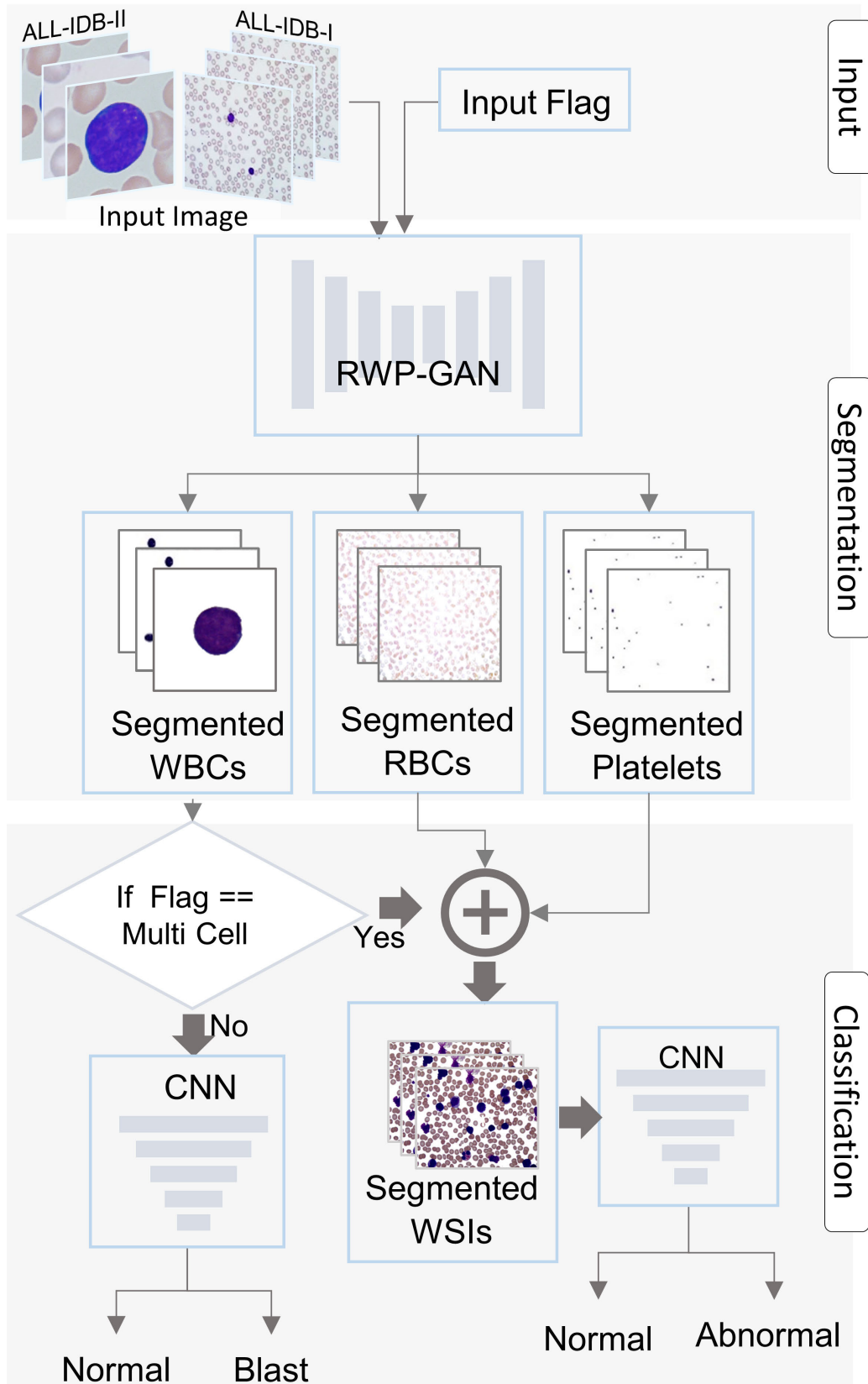


FIGURE 1. Data flow diagram of the proposed framework: For segmentation and classification of WBCs, RBCs, and PLTs. The framework receives two inputs: an image and a flag. The GAN then separates the three types of blood elements, after which a CNN model is employed to reorganize the image into its relevant class (healthy and non-healthy).

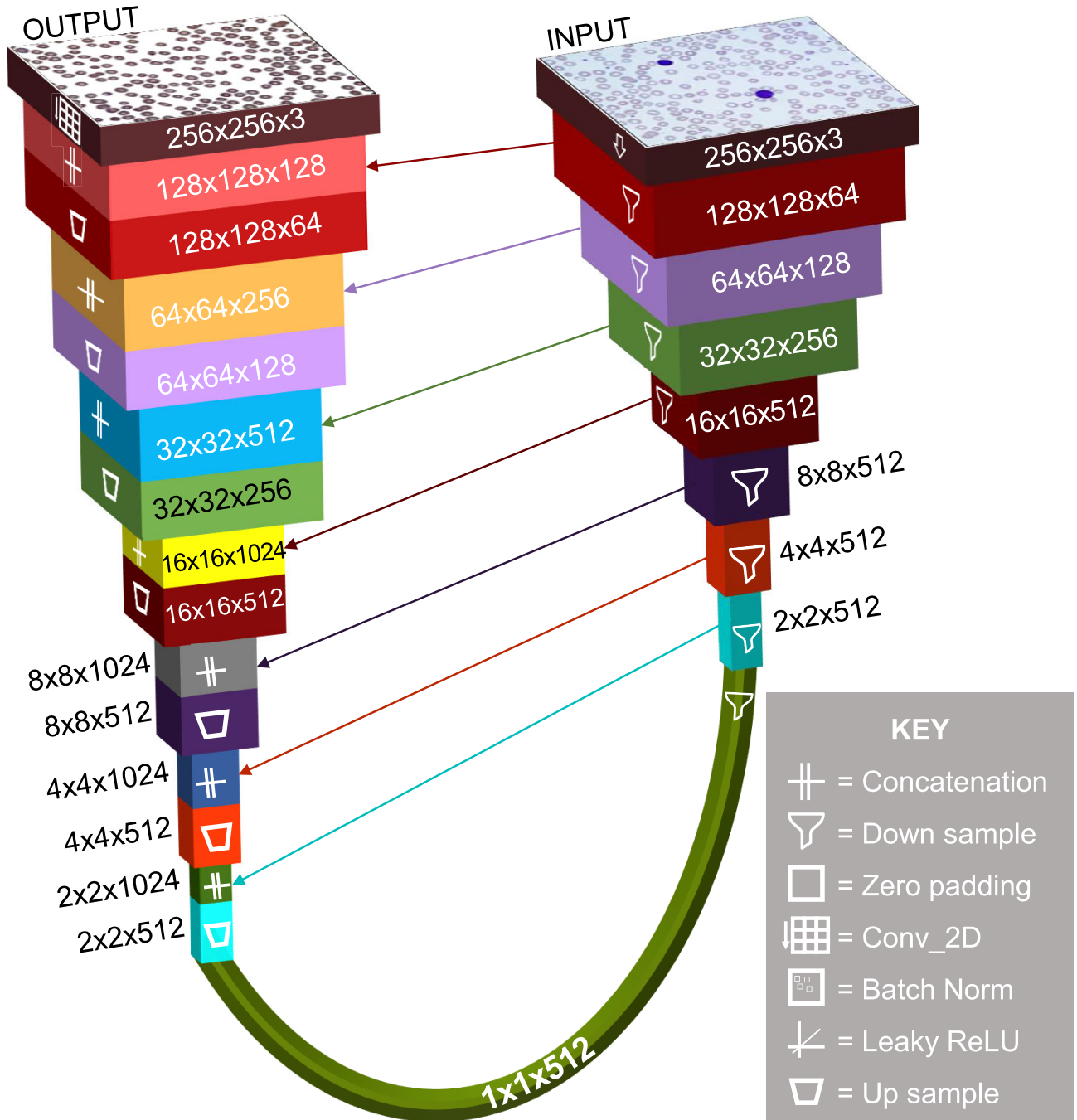


FIGURE 2. Internal structure of generator: The input of G starts from $256 \times 256 \times 3$ and reduces to $1 \times 1 \times 512$, and then $1 \times 1 \times 512$ is converted to $256 \times 256 \times 2563$ gradually.

between the input x and the Generator’s segmented target image $G(x, z)$.

A. NETWORK ARCHITECTURE

A GAN embodies competitively training of two adversarial networks: Generator and Discriminator. RWP-GAN portrays a modified version of U-Net [30]. The Generator of RWP-GAN comprises of encoding and decoding blocks with skip connections as shown in Figure 2.

1) GENERATOR

The Generator of RWP-GAN comprises eight encoding blocks. Each encoding block contains Leaky ReLU followed by batch normalization and convolution with stride 2. The convolution in each encoding block gradually down-samples the input from $256 \times 256 \times 3$ to $1 \times 1 \times 512$. On the other hand, RWP-GAN contains 7 decoding blocks. Each decoding block applies transposed convolution, batch normalization and ReLU, resulting in up-sampling of its input of size

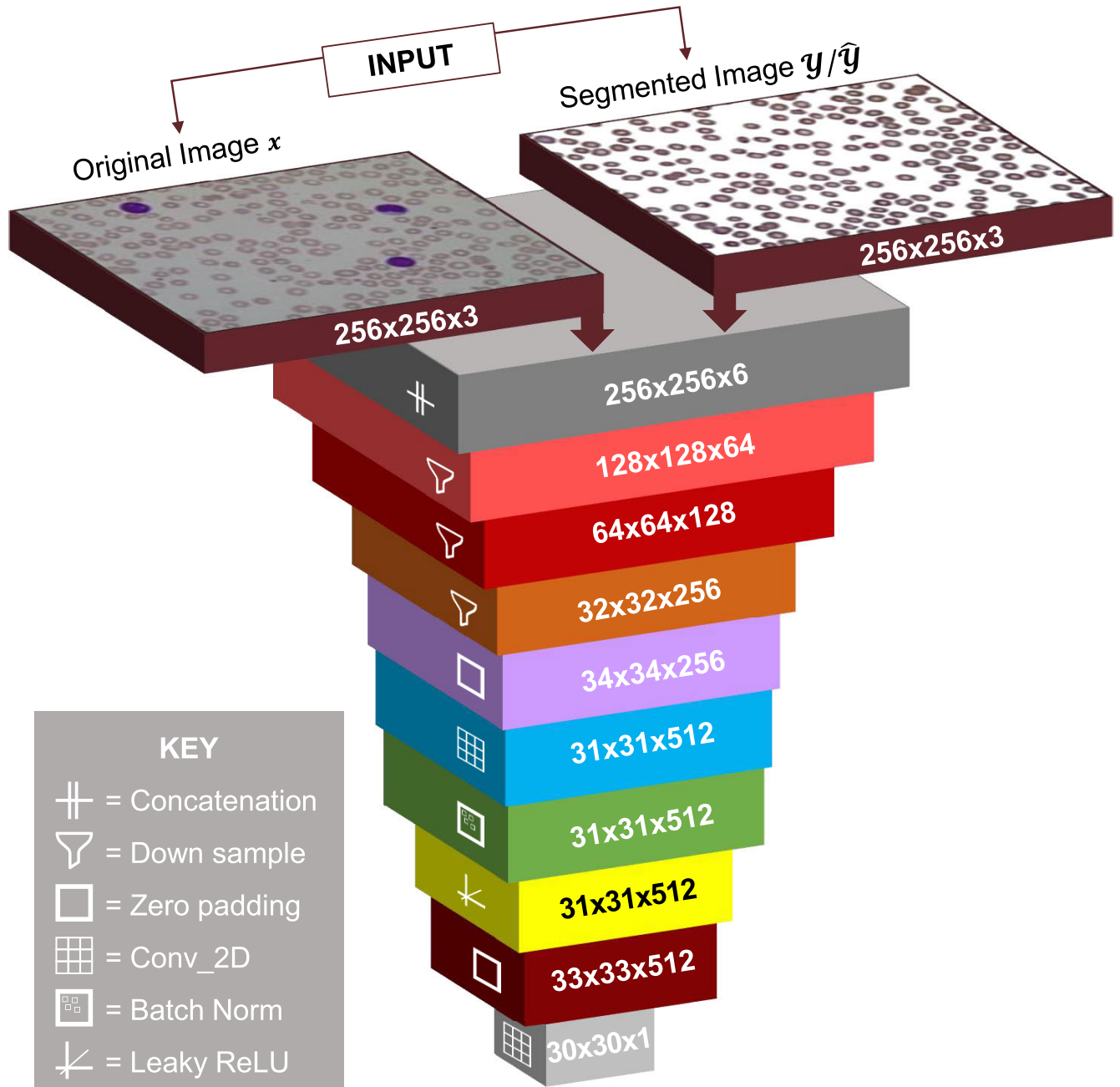


FIGURE 3. Internal structure of discriminator D : Block-level internal structure of the proposed Discriminator (D) that distinguishes the real from fake based on a single value representing the likelihood of the input image being real.

$1 \times 1 \times 512$ to $256 \times 256 \times 3$. However, a dropout of 0.5 was applied to the first three decoding blocks only. This dropout was applied after convolution and batch normalization before ReLU to achieve suitable noise removal while maintaining original cell features. Each decoding block was concatenated to the corresponding same-sized encoding block to achieve effective segmentation, as shown in Figure 2. The Generator accumulates 54,414,979 trainable parameters and 10880 non-trainable parameters out of 54,525,859.

2) DISCRIMINATOR

The Discriminator of RWP-GAN takes the generated image from the Generator and the real image from the dataset and tries to distinguish between them. The decision process involves the calculation of the probability of the input image being real or fake. The output of the Discriminator is a single value representing the likelihood of the input image being real. The Discriminator tries to maximize this value for real images and minimize it for generated images. In other words, it tries to classify the input image as either real or

fake based on the learned features. The proposed framework's Discriminator comprises three encoding blocks similar to that of the encoding blocks of the Generator. A separate convolution is applied after three encoding blocks with stride 1. Afterward, another similar convolution with stride 1 is applied, followed by batch normalization and Leaky ReLU. Finally, the generated image of Discriminator with size $30 \times 30 \times 1$ will be used for the decision of fakeness or originality, as shown in Figure 3. The Discriminator has 27,68,641 trainable parameters and 1,792 non-trainable parameters out of 2,770,433 parameters in total.

B. WORKING PIPELINE

The proposed technique's working pipeline comprises two main phases as shown in Figure 1: the first phase is segmentation and the second phase is classification. The *segmentation phase* consists of three segmentation networks based on RWP-GAN. Three RWP-GANs are trained for each cell type on E-ALL-IDB-I. Each segmentation network performs independent segmentation of blood cell types: RBC, WBC and PLTs. The segmentation phase uses two databases, E-ALL-IDB-I for all three types of cells while E-ALL-IDB-II for WBCs only. The segmentation phase categorizes all three types of cells and shows results on a single WSI for better assisting pathologists. In the segmentation phase, a distinct flag is fed with each test input image to direct the system to which cell type segmentation is required for the input image. The segmentation phase also shows segmented images of each cell type separately to help the pathologists identify diseases. The *classification phase* uses the E-ALL-IDB-I database to classify segmented WSIs into healthy and non-healthy samples. In contrast, the E-ALL-IDB-II database is used to classify WBCs into healthy and blast cells. Pre-trained ResNet-50, ResNet-101, and Mobile-Net are trained for classification to take advantage of transfer learning. The overall working pipeline of the proposed framework is shown in Figure 1.

C. RWP-GAN FOR SEGMENTATION

GAN is the first choice of researchers to generate artificial samples from randomly distributed data. For instance, a Google keyboard follows a similar mechanism to predict the suitable upcoming word written by the user. RWP-GAN comprises two neural networks: Generator (G) and Discriminator (D). Figure 6a shows the block diagram of the Generator (G) model. The key responsibility of G is to randomly generate artificial samples alike target sample but not exact. In Figure 6, a sample image and a respective target image are shown for understanding the training of Generator and Discriminator networks. In Figure 6, an input image is given to the adversary G for the generation of a new segmented image to fool D . G picks the random images from the training pool and creates respective segmented images by using real image features. To compare a generated and the target image, the mean absolute error is calculated using Equation 2. To compute the MAE for color images using

the RGB color space. The computation of MAE is done by taking the absolute difference between the predicted and ground truth pixel values and then taking the mean of all these absolute differences.

$$L_1 = MAE = \frac{1}{n} \sum_{i=1}^n |e_i| \quad \text{where } |e_i| = |\hat{y}_i - y_i| \quad (2)$$

Here, n is the number of pixels of image and e is the error between ground truth y and generated image \hat{y} . The Generator G accepts the criticism from the discriminator D during training to generate more realistic images. Sigmoid cross entropy is used to calculate the distance between true and false generated features as shown in Equation 2. After addition of entropy ratio and hyper-parameter lambda $\lambda = 100$ [29], [31], the outcome is used to find the area under curve (AUC) of correctly identified features for each image using gradients. Figure 2 and Figure 3 show the internal structure of whole GAN as Generator G and Discriminator D , respectively. During training, all trainable network parameters are gradually trained to transform the input image into the target image. In Figure 3, the Discriminator D accepts the generated (segmented) image from the Generator G along with the target image. The Discriminator D examines both the images by comparing the difference between the generated and the target image. Finally, the Discriminator D takes decision about the generated image with respect to the target image as shown in Figure 3. Suppose D makes the right decision to identify the real and fake images. In that case, G updates its weights and biases to perform effective artificial segmentation to defeat D . If D makes a wrong decision between the identification of real and fake images, then D updates its weights and biases to detect better the fake images generated by G .

IV. RESULTS AND DISCUSSION

This section discusses the database description, training process, and loss functions of RWP-GAN. Loss functions were calculated for Generator and Discriminator. For evaluation of segmentation results, we use the following metrics: SSIM, PSNR, SNR, PCE, and PCC. The accuracy of each classification model for the images in the two databases is calculated for classification.

A. DATABASE DESCRIPTION

For segmentation, RWP-GAN uses two databases, (1): Extended Acute Lymphoblastic Leukemia Image Database-I (E-ALL-IDB-I) that contains all types of blood cells, viz., RBCs, WBCs and PLTs, and (2): E-ALL-IDB-II that contains only a single WBCs.

1) E-ALL-IDB-I

As E-ALL-IDB-I contains multiple WBCs, it is impossible to classify the whole image as Normal or Blast Cells. However, E-All-IDB-I's whole image can be classified as Normal and Abnormal after the segmentation. To validate

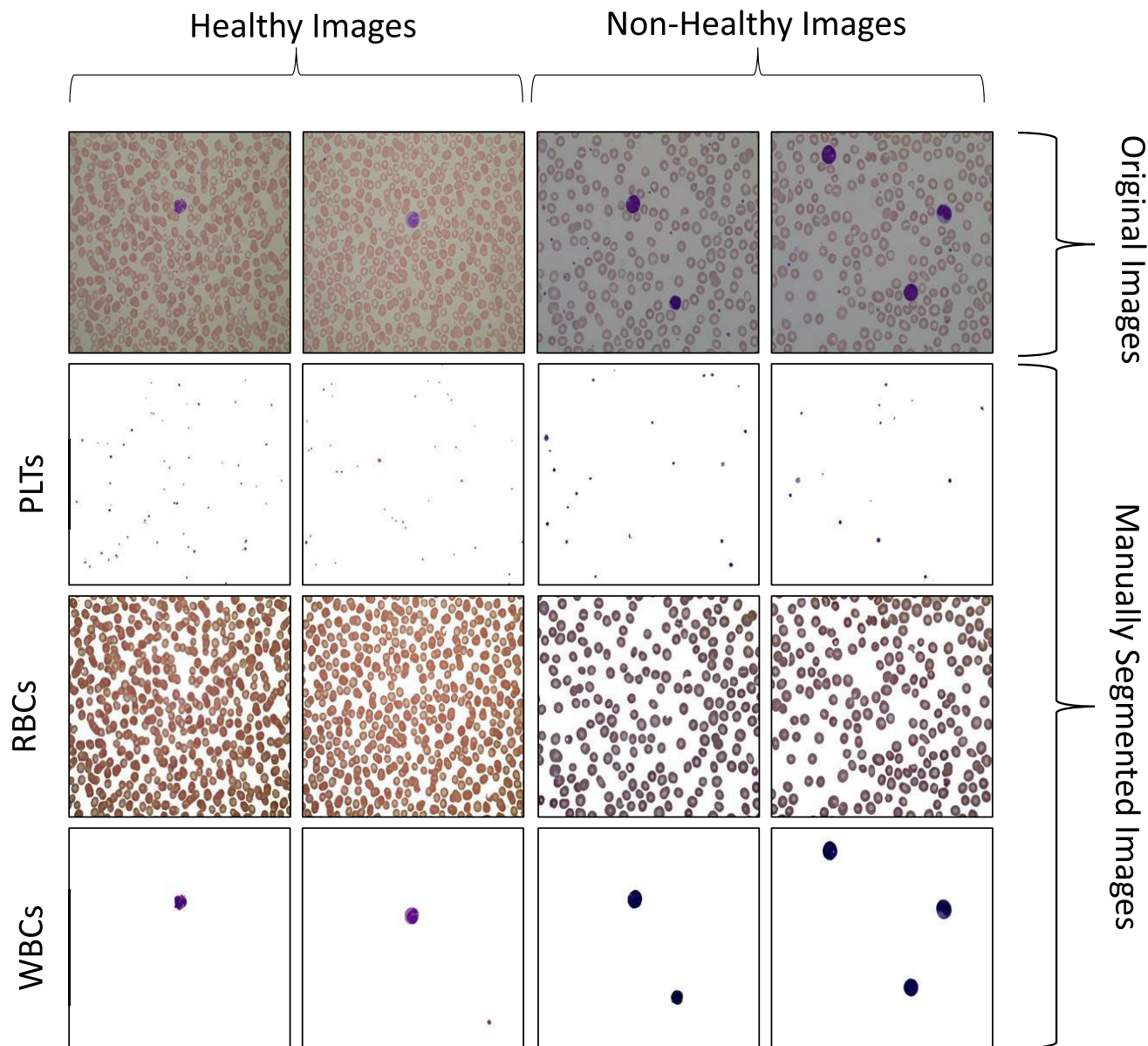


FIGURE 4. The samples images from the E-ALL-IDB-I database: The first two columns display images of healthy individuals while the last two columns show images of non-healthy patients. The first row shows the original images while the second, third, and fourth rows show the manually segmented PLTs, RBCs, and WBCs, respectively, corresponding to the original images.

the segmentation performance of RWP-GAN, we use E-ALL-IDB-I [4]. The base ALL-IDB-I database consists of 108 images. Out of 108 images, 49 images belong to non-healthy patients, while 59 images belong to healthy patients. The E-ALL-IDB-I database consists of all original images from ALL-IDB-I and their manually segmented images for each type of cell. In this way, the total number of images in the E-ALL-IDB-I database becomes 432, 108 original images, 108 segmented RBCs, 108 segmented WBCs, and 108 segmented PLTs. Hence, the new database consists of 390,000 segmented blood cells from all images. Figure 4 shows sample images form E-ALL-IDB-I database.

2) E-ALL-IDB-II

In contrast, E-ALL-IDB-II (E-ALL-IDB-II) segmented WBC can be classified into Blast and Normal cells. To validate the classification performance after using RWP-GAN, E-ALL-IDB-II is used. The base ALL-IDB-II [32] database has been specifically designed for classification purposes. ALL-IDB-II data-base comprises 260 cropped images of WBCs from ALL-IDB-I. Images from “all” patients are named ImXXX-Y.jpg, with Y=1 and Y=0 representing images from affected and healthy individuals, respectively. We have generated 260 individual WBCs as ground truth and pixel-level labeling for classification and have also combined leukocytes/erythrocytes ground truth, as shown in Figure 5.

In Figure 5, four random samples from the E-ALL-IDB-II dataset are shown. Row-1 indicates the original from the base dataset. Row-2 indicates the pixel-level ground truth of WBCs, while Row-3 shows the pixel-level ground truth of RBCs.

3) AUGMENTATION

I used data augmentation techniques such as cropping, flipping, and rotation to expand the E-ALL-IDB-I and E-ALL-IDB-II datasets artificially. Initially, the E-ALL-IDB-I consists of 108 original images and 108 segmented images of RBC, WBC, and Platelets. So the total initial dataset counts become 432. After applying augmentation, each image of the ALL-IDB-I dataset is converted into 08 different versions of images. So the total images become $432 \times 8 = 3456$. This helped to prevent overfitting by making the model less sensitive to small changes in the data. While in the case of ALL-IDB-II, the same procedure was applied, and the total number of images became $260 \times 8 = 2080$. Finally, I used a validation set of 20% of the data to evaluate the model's performance. This helped us to identify the overfitting of the training data (if any).

B. TRAINING PROCESS

Generally, the training process of GANs is based on a minimax game between the generator and the discriminator. The generator tries to produce images that look like real data, while the discriminator tries to distinguish between real and fake images. The goal of the generator is to maximize the probability of the discriminator making a mistake, while the goal of the discriminator is to minimize that probability. The two components are trained alternately using gradient descent, where the generator updates its parameters based on the feedback received from the discriminator, and the discriminator updates its parameters based on the feedback from the real and fake images. The role of the discriminator in providing feedback to the generator is important for the success of GANs. The discriminator acts as a teacher for the generator, telling it how well or how poorly the generator generates the images. The discriminator provides feedback to the generator in the form of a loss function, which measures how far the generated images are from the real data distribution. The loss function can be different depending on the type of GAN, but in general, it penalizes the generator for producing images that are easily classified as fake by the discriminator. The generator then uses this feedback to improve its image quality by adjusting its parameters in such a way that reduces the loss. In the context of blood cell segmentation, GANs can use the discriminator to provide feedback to the generator on how realistic synthetic images of blood cells are generated. For example, suppose the generator produces an image of a blood cell that does not match the given label or attribute, such as cell type. In that case, the discriminator can give a high loss to the generator, indicating that it has failed to satisfy the condition. Similarly, if the generator produces an image of a blood cell that does not look

like a real blood cell. In that case, the discriminator can also give a high loss to the generator, indicating that it has failed to capture the data distribution. The generator can then use this feedback to generate better images of blood cells that match both the condition and the data distribution.

Usually, GAN follows the generative learning of map from randomized noise vector z to final image y , $G : z \rightarrow y$ [19]. While the proposed RWP-GAN learns map from randomized noise vector z along with ground truth image x to construct the output image y , $G : x, z \rightarrow y$. Training the Discriminator D adversarially enables D to detect real versus fake images. In this way, the Generator G generates an image similar to the real one and indistinguishable from the target image. Figure 6 depicts training mechanism of the proposed RWP-GAN for segmentation. Dropout of 0.5 is added to reduce the noise. To achieve effective segmentation, RWP-GAN uses Adam stochastic gradient descent method [33] for optimization with learning rate of 0.0002 and momentum estimates of β_1 and β_2 as 0.5 and 0.999, respectively.

Selecting an appropriate number of epochs is a critical aspect of training in machine learning models such as the RWP-GAN. This decision hinges on converging the model's performance and avoiding overfitting. In the context of RWP-GAN, the number of epochs has been chosen carefully, considering the complexities associated with different blood cell types. For RBCs and WBCs segmentation, 350 epochs have been determined as an optimal balance between convergence and overfitting. During these epochs, the model progressively refines its segmentation ability while avoiding excessive fine-tuning that could lead to fitting noise in the training data. In contrast, PLTs, being the smallest and most intricate blood cells, necessitate a more extended training duration. Hence, a higher number of epochs, 500, has been allocated to the segmentation model for PLTs. This extended training period allows the model to better comprehend the nuanced features of PLTs, enabling accurate and robust segmentation. The batch size of 1 has been chosen for segmentation across all cell types. This decision ensures that each cell image is treated individually during training, reducing potential biases stemming from batch processing and enabling the model to learn distinct features of each cell type. Regarding computational considerations, the training times for RBCs and WBCs are approximately 120 minutes each, while PLTs require 170 minutes on a single P100s GPU. These durations strike a balance between computational efficiency and model accuracy. During testing, the RWP-GAN demonstrates remarkable efficiency, with a test time of only 0.3 seconds for each type of image on the same GPU, showcasing the model's real-time application potential. For classification, the input size requirements of ResNet-50, ResNet-101, and MobileNetV2 are standardized at $224 \times 224 \times 3$. Random crops of this size are generated from segmented databases, E-ALL-IDB-I and E-ALL-IDB-II, ensuring diverse training samples and generalization capacity. Moreover, a pre-trained model with a batch size of 128 and a learning rate of 0.0001 is employed for classification tasks. This transfer

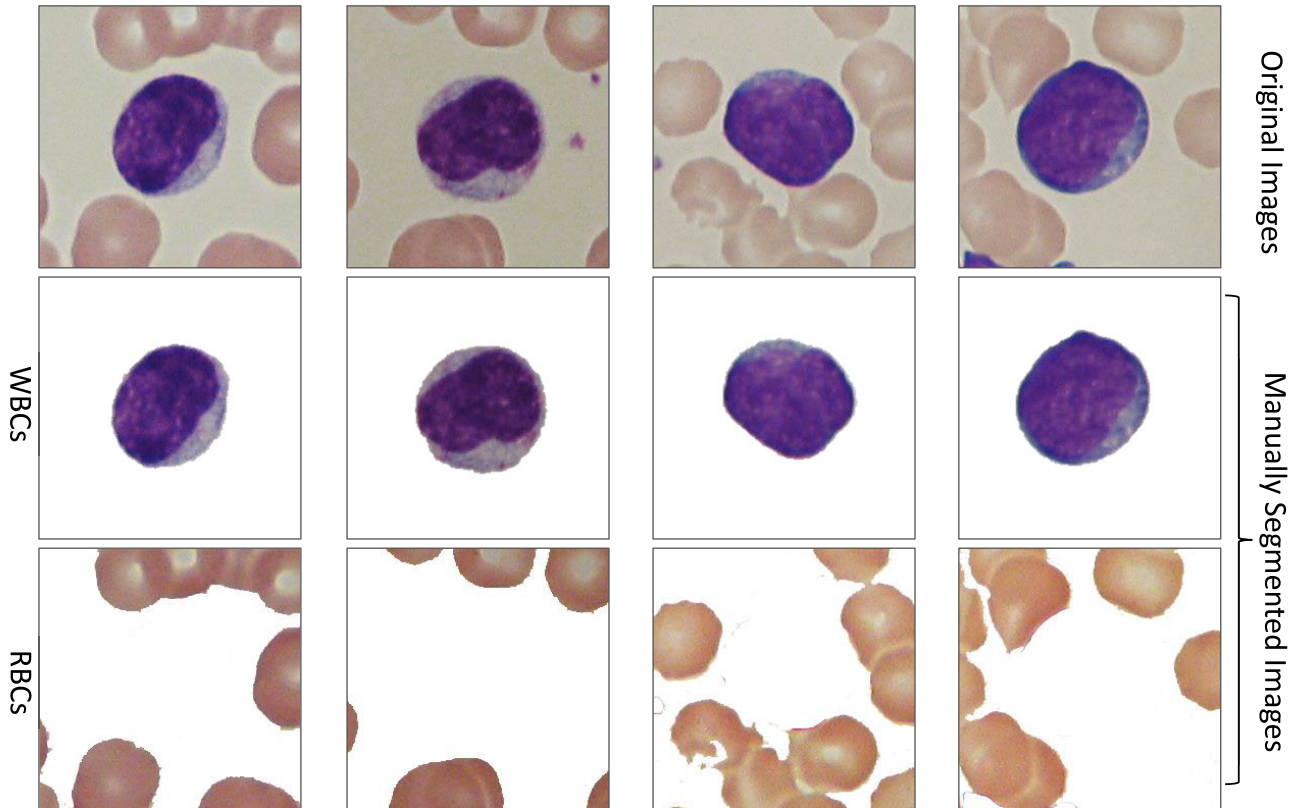


FIGURE 5. Cropped WBCs and RBCs: Ground truth and pixel-level labelling of cropped WBCs and RBCs. Row-I represents original image, Row-II shows the pixel-level ground truth of WBCs, and Row-III indicates pixel-level ground truth of RBCs.

learning approach leverages existing knowledge, leading to enhanced classification performance. The use of the stochastic gradient descent optimization method supports iterative model updates for improved convergence.

C. LOSS FUNCTIONS

1) GENERATOR LOSS L_G

Generator loss L_G is the sigmoid cross entropy loss in Equation 3 regarding the generated image. MAE (mean absolute error) in Equation 2 is considered as L_1 loss between the machine segmented and the manually segmented image. L_1 loss regulates the Generator for generating images similar to manual segmented images. The addition of L_1 loss in conditional adversarial loss is regulated by a hyper-parameter Lambda [26],

$$L_G = \frac{1}{n} \sum_{i=1}^n y_i \cdot \log \hat{y}_i + (1 - y_i) \cdot \log (1 - \hat{y}_i) \quad (3)$$

where \hat{y}_i is the i -th generated value in the RWP-GAN output, y_i is the respective manually segmented value, and n is the number of generated values in the RWP-GAN output. Hence, the total Generator loss (L_{GT}) can be expressed by Equation 4, where the value of Lambda is set to 100 as suggested in [29]. Initially, when we set hyper-parameter lambda = 0, the loss function leads to sharper results, but it also introduces visual artifacts in certain cells of the blood images. Subsequent to this, the lambda value is incremented from 0 to 100,

resulting in enhanced model performance, with the most optimal outcomes observed at lambda = 100.

$$L_{GT} = L_G + (\lambda * L_1) \quad (4)$$

In our experimental results, Generator losses of WBCs, RBCs, and PLTs start from 2.66, 0.86 and 1.44, respectively, as shown in Figure 7a. These losses approaches to zero by maximizing the $\log(\hat{y})$ as shown in Equation 1. Maximizing function $\log D(x, \hat{y})$ tries to improve the ability of the Generator to generate images near to manually segmented images to fool the Discriminator. As the training goes ahead, Generator's learning rate increases with the reduction in the loss that ultimately approaches zero. The Generator increases its learning rate to generate plausible instances considering joint probability $P(x, y)$. RWP-GAN achieved the best training results at 350 epochs in the case of WBCs and RBC. However, in the case of PLTs being complex in nature and small in size, the best training results are obtained at 500 epochs. Generator total loss L_{GT} in Figure 8 shows immediate trend towards zero for WBC and RBCs. In contrast, the graph shows the relatively diverse trend for PLTs due to complex shape and small size.

2) DISCRIMINATOR LOSS L_D

The discriminator loss increases gradually with training. The Discriminator takes two inputs: manual segmented (real) image and machine segmented (generated) image. The real

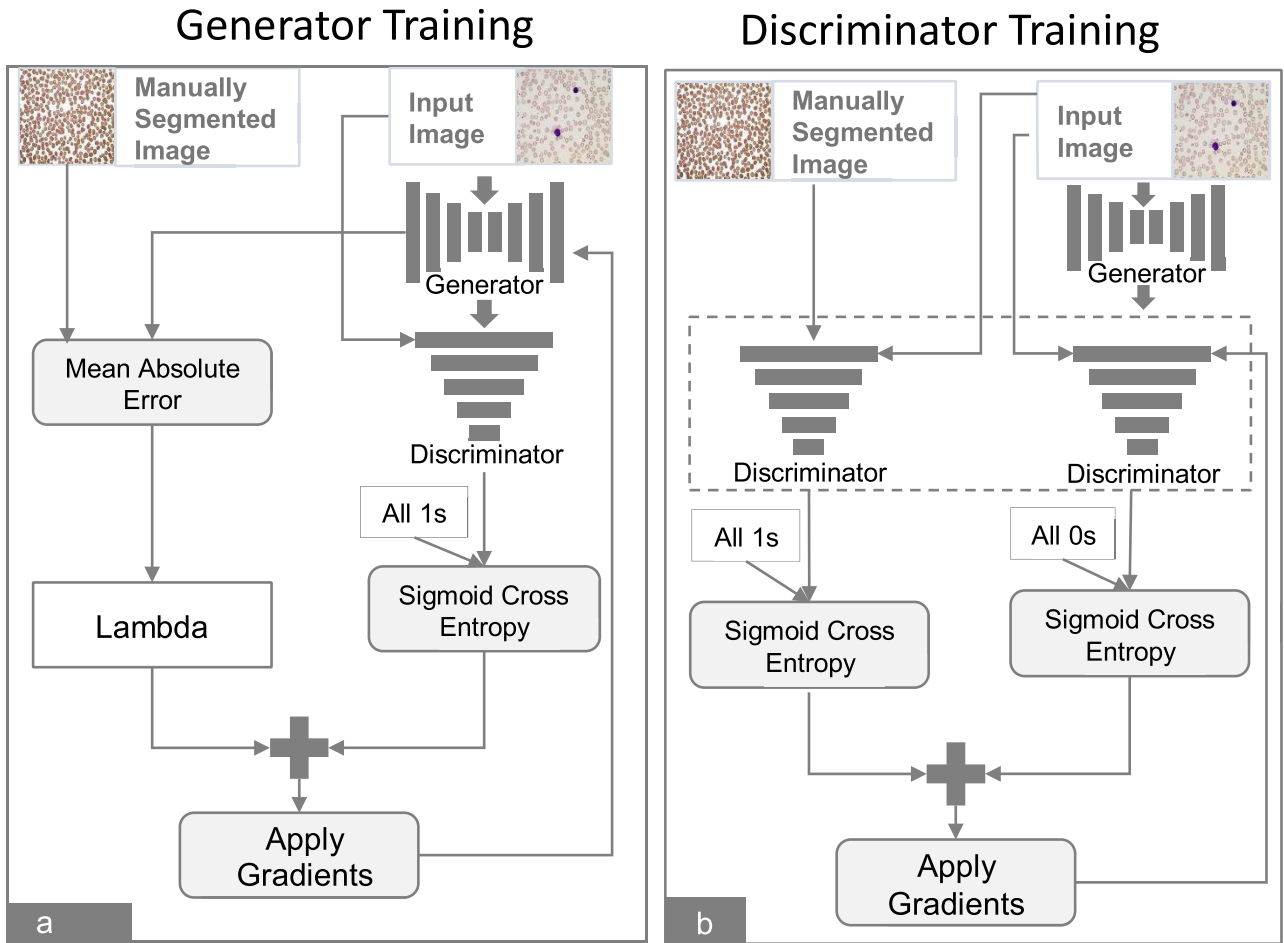


FIGURE 6. Block diagram of (a) Generator (G), and (b) Discriminator (D): Part a shows the training process of generator while part b indicates the training process of discriminator. Real images are indicated by all 1s in the figure, while generated/fake images are indicated by all 0s.

loss is a sigmoid cross entropy loss of real images and generated images. The generated loss is a sigmoid cross entropy loss of the generated images, and an array of zeros representing all the machine-generated images are fake. While an array of ones represents all the real images. Hence, the total Discriminator loss L_{DT} is the sum of real loss L_R and generated loss L_G as shown in Equation 5. During the discriminator process, an array of ones represents the original segmented image, while arrays of zeros represent the machine-generated segmented image.

$$L_{DT} = L_G + L_R \tag{5}$$

The Discriminator D tries to maximize the $\log(D(x))$ to beat the Generator. In our experiments, L_D curves of WBCs, RBCs, and PLTs start at 1.33, 1.38, and 1.04, respectively, and decreases with the increase of epochs as shown in Figure 7b. At the beginning of training, the Discriminator was able to accurately classify the generated images of white blood cells as fake, indicating that the Generator was not yet producing realistic images. However, the Discriminator was not able to accurately classify the generated images of

red blood cells and platelets, which means that the Generator was producing more realistic images of those types of cells. As training progressed, the Discriminator became better at classifying all types of generated images as fake, which suggests that the Generator was improving and producing more realistic images overall. So with the passage of time, the learning ability of $\log(D(G(z)))$ increases and G generates data instances that are more closer to the ground truth. However, D also maximizes $\log(D(x))$ to discriminate between real and generated instances. For WBCs and PLTs, L_D loss curve moves downward rapidly with the progress of training process. The L_D curve of RBCs is initially high but moves downward after 400 epochs as shown in Figure 7a.

3) LOSS EXTREMA

Table 1 presents statistical information on the maximum, minimum, and average losses for each category of blood cell images. In particular, columns 2, 3, and 4 show the maximum, average, and minimum losses for RBCs, WBCs, and PLTs, respectively. These values provide insight into the performance of the discriminator and generator

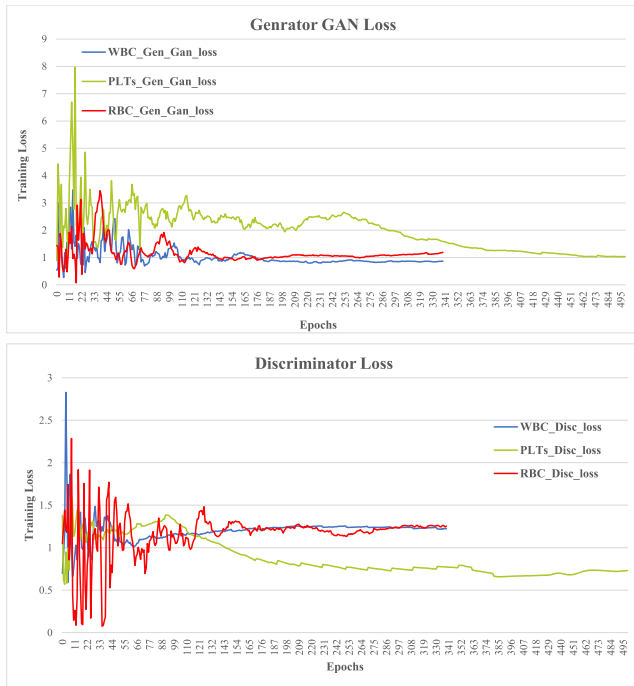


FIGURE 7. GAN generator and discriminator losses: Training losses for WBCs, RBCs, and PLTs in the GAN generator and discriminator are shown on the Y-axis, with the number of epochs displayed on the X-axis.

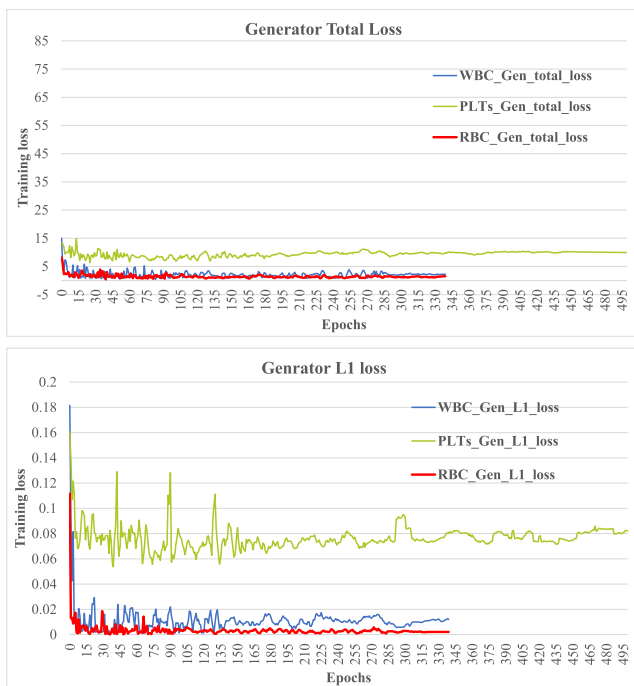


FIGURE 8. Generator total and generator L₁ loss: The Y-axis shows the training losses for the generator total and generator L₁ loss of WBCs, RBCs, and PLTs in the figure, with the number of epochs displayed on the X-axis.

models when dealing with each category of blood cell images. By examining these statistics, we can gain a better

understanding of which categories the models struggled with and which categories they performed well on.

4) **DISCRIMINATOR LOSS – MAXIMUM ($L_{D(MAX)}$), AVERAGE($L_{D(AVG)}$), AND MINIMUM ($L_{D(MIN)}$)**

Results in Table 1 reveal that $L_{D(max)}$ of RBCs, WBCs, and PLTs is 3.46, 2.83, and 4.17, respectively. These losses reduce up to 0.81, 1.22, and 1.16 for average case $L_{D(avg)}$, while minimum loss $L_{D(min)}$ during the whole training process is 0.08, 0.36, and 0.03 for RBC, WBC, and PLTs. In Table 1, results show that proposed framework reduces Discriminator loss from 3.46 to 0.08 for RBCs, 2.83 to 0.36 for WBCs, and 4.17 to 0.03 for PLTs.

5) **GENERATOR LOSS – MAXIMUM ($L_{G(MAX)}$), AVERAGE($L_{G(AVG)}$), AND MINIMUM ($L_{G(MIN)}$)**

Table 1 shows the maximum Generator loss $L_{G(max)}$ of RBCs, WBCs, and PLTs with values of 7.97, 3.63, and 3.59, respectively. $L_{G(avg)}$ shows 1.99, 1.02, and 1.18 while $L_{G(min)}$ was 0.09, 0.14, and 0.07 for RBCs, WBCs, and PLTs, respectively. Results shows that the proposed framework reduces Generator loss from 7.97 to 0.09 for RBCs, 3.63 to 0.14 for WBCs, and 3.59 to 0.07 for PLTs.

6) **L₁ LOSS – MAXIMUM ($L_{1(MAX)}$), AVERAGE($L_{1(AVG)}$) AND MINIMUM ($L_{1(MIN)}$)**

Results in Table 1 show that $L_{1(max)}$ of RBCs, WBCs, and PLTs is 0.47, 0.04, and 0.02, respectively. These losses reduce up to 0.08, 0.01 and 0.004 for $L_{1(avg)}$ case, while $L_{1(min)}$ during the training process is 0.04, 0.0005, and 0.00001 for RBCs, WBCs, and PLTs, respectively. The Discriminator of RWP-GAN provides a probability that indicates either the input image is Generator output or manually segmented image. As Discriminator classifies the input image as manually segmented image or GAN-generated image, the Generator uses this feedback to improve the weights of the network. During the training process, the Loss L1 reduces from 0.47 to 0.04 for RBCs, 0.04 to 0.0005 for WBCs, and 0.02 to 0.00001 for PLTs as shown in Table 1.

7) **GENERATOR TOTAL LOSS – MAXIMUM ($L_{GT(MAX)}$), AVERAGE($L_{GT(AVG)}$) AND MINIMUM ($L_{GT(MIN)}$)**

Table 1 shows that the maximum Generator total loss $L_{GT(max)}$ of RBCs, WBCs, and PLTs is 16.90, 5.80, and 3.88, respectively. Table 1 shows $L_{GT(avg)}$ of 9.50, 2.09, and 1.48 while $L_{GT(min)}$ is 4.72, 0.41, and 0.25 for RBCs, WBCs, and PLTs, respectively. Results reveals that the proposed framework reduces the Generator total loss from 16.90 to 4.72 for RBCs, 5.80 to 0.41 for WBCs, and 3.88 to 0.25 for PLTs. In the nutshell, above discussion discloses that the proposed GAN architecture outperforms to reduce the Generator total loss of RBCs by 12.18, 5.39 for WBCs, 3.62 for PLTs.

In addition to the given information, it can be mentioned that the reduction in Generator total loss for each cell type indicates the effectiveness of the proposed GAN architecture

TABLE 1. Average losses of WBCs, RBCs and platelets.

Loss	RBC	WBC	Platelets	Quantity
Discriminator	3.4679773	2.8275466	4.1777401	Maximum
Generator	7.9675803	3.6282313	3.5938938	
L1	0.4727152	0.0419668	0.0185975	
Generator Total	16.9016571	5.8090472	3.8780067	
Discriminator	0.8108084	1.2191777	1.1596827	Average
Generator	1.9937623	1.0230852	1.1767873	
L1	0.0776031	0.0113782	0.0040520	
Generator Total	9.4991832	2.0890610	1.4771987	
Discriminator	0.0855512	0.3563231	0.0285471	Minimum
Generator	0.0901551	0.1451996	0.0742086	
L1	0.0443960	0.0004655	0.0000116	
Generator Total	4.7203627	0.4102790	0.2525901	

TABLE 2. Segmentation evaluation parameters.

Parameters	SSIM	PSNR	SNR	PCE	PCC
RBC-Train	0.898249	24.28066	22.33475	0.068064	0.931936
RBC-Test	0.899502	21.23045	18.28898	0.065572	0.934430
WBC-Train	0.979361	35.20181	35.02372	0.003328	0.996672
WBC-Test	0.977765	34.38795	34.35404	0.001668	0.998332
PLTs-Train	0.984245	37.21119	37.20387	0.000523	0.999485
PLTs-Test	0.956539	31.81141	31.80071	0.000979	0.999021

in generating more realistic and accurate images. This reduction in loss can be attributed to the use of transfer learning and the incorporation of L1 loss in the objective function, which helps in preserving the structural information of the cells in the generated images. Furthermore, it can be stated that the proposed framework can be used as a promising tool for generating synthetic blood cell images, which can aid in various medical applications such as training and testing of computer-aided diagnosis systems, and in education and research.

D. SEGMENTATION EVALUATION PARAMETERS

For evaluation of the segmented images, proposed work analyze manual-segmented images versus machine-generated segmented images using five statistical image quality parameters. The parameters include SSIM, PSNR, SNR, PCE and PCC.

1) STRUCTURAL SIMILARITY SSIM

The SSIM index or quality assessment index is based on the computation of three terms: (i) Luminance: light intensity, (ii) Contrast: Make object distinguishable from background and (iii) Structural: Structure of objects in image. The overall index is a multiplicative combination of these three terms with ground truth image (g) and predicted/generated image

(p) as shown in Equation 6.

$$SSIM(g, p) = [l(g, p)]^\alpha \cdot [c(g, p)]^\beta \cdot [s(g, p)]^\gamma \tag{6}$$

Here the SSIM is further explain in Equation 7.

$$l(g, p) = \frac{2\mu_g\mu_p + C_1}{\mu_g^2\mu_p^2 + C_1},$$

$$c(g, p) = \frac{2\sigma_g\sigma_p + C_2}{\sigma_g^2\sigma_p^2 + C_2},$$

and $S(g, p) = \frac{\sigma_{gp} + C_3}{\sigma_g\sigma_p + C_3}$ (7)

where $\mu_g, \mu_p, \sigma_g, \sigma_p,$ and σ_{gp} are the local means, standard deviations, and cross-covariance for ground truth images (g) and predicted/generated images (p). If $\alpha = \beta = \gamma = 1$ (the default for exponents), and $C3 = C2/2$ (default selection of C3) the index simplifies in Equation 8:

$$SSIM(g, p) = \frac{(2\mu_g\mu_p + C_1)(2\sigma_{gp} + C_2)}{(\mu_g^2 + \mu_p^2 + C_1)(\sigma_g^2 + \sigma_p^2 + C_2)} \tag{8}$$

The proposed framework achieves a highest SSIM of 98.42% in PLTs training on 90 images while test SSIM comes out to be 95.65% on 18 randomly selected images as shown in Table 2. The RBCs SSIM values are 89.82% for training and 89.95% for testing, whereas WBCs SSIM values are 97.93% for training and 97.77 for testing as shown in Figure 9.

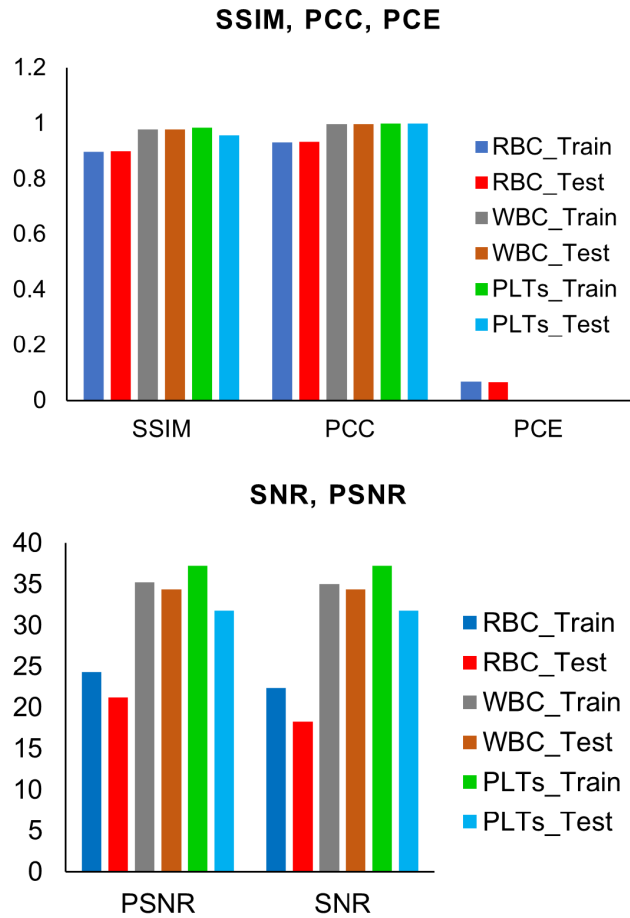


FIGURE 9. Segmentation evaluation parameters: The figure displays the segmentation evaluation parameters for testing and training of WBCs, RBCs, and PLTs.

2) PEAK SIGNAL-TO-NOISE RATIO (PSNR)

The PSNR function implements the following equation to calculate the Peak Signal-to-Noise Ratio (PSNR) and Expressed in Equation 9:

$$PSNR = 10 \cdot \log_{10} \frac{R^2}{MSE} \quad (9)$$

and MSE is shown in Equation 10.

$$MSE = \frac{1}{n} \sum_{i=1}^n (g_i - p_i)^2 \quad (10)$$

where R is the Peak value, which is either specified by the user or taken from the range of the image datatype (e.g., in case of image it is 255). MSE is the mean square error, that is, MSE between g and p , where g is the ground truth image, p is the predicted or newly generated image, and n is the total number of pixels. Results in Table 2 indicate that the PSNR of the proposed GAN architecture is in the range of 21.23 (RBC Test) to 37.21 (PLTs Train). PSNR for RBCs, WBCs, and PLTs is 21.23 to 24.28, 34.38 to 35.20, and 31.81 to 37.21 for testing and training, respectively, as shown in Figure 9.

3) SIGNAL-TO-NOISE RATIO (SNR)

The SNR is used in imaging to characterize image quality. The sensitivity of a (digital or film) imaging system is typically described in the terms of the signal level that yields a threshold level of SNR as shown in Equation 11.

$$SNR = 10 \cdot \log_{10} \frac{P_s}{P_n}, \quad (11)$$

where P_s is target image signal and P_n is the noise signal that we found in generated image. Results in Table 2 reveal that the overall SNR range is near to the PSNR, that is, 18.28 to 37.20 for all the three classes. Results also indicate that the individual SNR values for RBCs, WBCs, and PLTs is 18.28 to 22.33, 34.35 to 35.02, and 31.80 to 37.20, respectively.

4) PIXEL CLASSIFICATION ERROR (PCE)

The PCE is a ratio between the number of misclassified (n^o) pixels and the total number of pixels (n) within an image shown in Equation 12.

$$PCE = \frac{\sum n^o}{n} \quad (12)$$

The minimum PCE shows the minimum loss for training and testing of segmentation process. The proposed GAN achieves a minimum loss for PLTs class with 0.00098 to 0.00052 for test and train images. While this error was slightly higher in case of WBCs, that is, 0.00167-to-0.0033 for train and test images, RBCs show a highest PCE error, that is, 0.065 to 0.068 for train and test images as shown in Figure 9.

5) PIXEL CORRECTLY CLASSIFIED (PCC)

The PCC is the ratio between correctly classified pixels (n_c) and the total number of pixels (n) shown in Equation 13.

$$PCC = \frac{\sum n_c}{n} \quad (13)$$

The proposed GAN framework achieves 99.948% to 99.902% accuracy for correct classification of train and test PLTs, respectively. Results indicate that the correct classification of WBCs during training and testing is 99.67% and 99.83%, respectively. Additionally, results indicate that the PCC for RBCs is 93.19% and 93.44% for training and testing images, respectively, as shown in Figure 9.

Proposed method automatically extracts the segmented area and examine the outlines of each blood cell element. This phenomenon helps to detect the local and subtle variations. RWP-GAN based on an adversarial network that capture the pixels of major portion of an image instead of targeting only neighboring pixels. Due to the larger receptive field, it extracts more global information. This helps to capture higher-order statistical consistency, i.e., neither enforced in pixel-wise loss nor measured in conditional random fields using pairwise loss. This approach makes the proposed model more context-aware that ultimately leads to best results.

Table 4 presents a comparison of our proposed GAN flavors with existing ones, which typically utilize generalized datasets rather than specific medical datasets. Our work

introduces new GAN flavors that incorporate a structured context-aware loss, resulting in more promising results for complex and sensitive medical image data. This approach recognizes the unique challenges presented by medical datasets and aims to address them with modified GAN techniques for blood cells segmentation.

E. GAN EVALUATION MATRICES

To evaluate the RWP-GAN network, we have used several GAN evaluation matrices, i.e., Fréchet Inception Distance (FID) Equation 14, Inception Score (IS) Equation 15, Perceptual Similarity Index (PSI) Equation 16, Kernel Inception Distance (KID) Equation 17, and Wasserstein Distance (WD) Equation 18. The mathematical formulation of each matrix is given below.

1) FRÉCHET INCEPTION DISTANCE (FID)

FID measures the similarity between two Gaussian distributions, one representing real images and the other representing generated images. Lower FID values indicate closer distribution similarity.

$$FID = \|\mu_r - \mu_g\|^2 + \text{Tr}(\Sigma_r + \Sigma_g - 2(\Sigma_r \Sigma_g)^{1/2}) \quad (14)$$

Here, μ_r and μ_g are the mean feature vectors of real and generated images. Σ_r and Σ_g are the covariance matrices of real and generated images, respectively. While Tr denotes the trace operation.

2) INCEPTION SCORE (IS)

IS measures the quality and diversity of generated images based on how well they fool a pre-trained classifier and their entropy. Higher IS values indicate better image quality and diversity.

$$IS = \exp(\mathbb{E}_x [D_{KL}(p(y|x)||p(y))]) \quad (15)$$

Here, x represents an image, y is the label predicted by the classifier, $p(y|x)$ is the conditional class distribution given an image x , $p(y)$ is the marginal class distribution, and D_{KL} denotes the Kullback-Leibler divergence.

3) PERCEPTUAL SIMILARITY INDEX (PSI)

PSI computes the perceptual similarity between real and generated images using a pre-trained neural network’s feature representations. Lower PSI values indicate higher perceptual similarity.

$$PSI = \frac{1}{N} \sum_{i=1}^N \|f(x_i) - f(G(z_i))\|_2 \quad (16)$$

Here, N is the number of image pairs, x_i is the i -th real image, z_i is the i -th random noise vector, G is the generator, and $f(\cdot)$ is the feature extraction function of the pre-trained neural network.

TABLE 3. Comparison of GAN models on the ImageNet dataset.

GAN Network	FID	IS	PSI	KID	WD
CGAN [35]	26.2	2.19	0.77	20.6	10.6
InfoGAN [36]	25.5	2.24	0.79	19.8	10.2
ACGAN [37]	24.8	2.3	0.81	19	9.8
DRIT [38]	23.9	2.37	0.83	18.2	9.4
MUNIT [39]	23.1	2.44	0.85	17.4	9
BigGAN [40]	21.9	2.56	0.88	16.2	8.4
StyleGAN2 [41]	18.4	3.35	0.93	14.1	7.4
StyleGAN2-ADA [42]	17.5	3.48	0.95	13.6	7.1
BigGAN-deep [43]	17.8	3.43	0.94	13.9	7.2
Imagen [44]	16.6	3.61	0.96	12.8	6.8
RWP-GAN (Proposed)	16.4	3.7	0.91	12.3	6.5

4) KERNEL INCEPTION DISTANCE (KID)

KID computes the distance between feature representations of real and generated images using kernel methods. Lower KID values indicate better image quality.

$$KID = \frac{1}{N^2} \sum_{i,j} k(f(x_i), f(x_j)) - \frac{2}{N^2} \sum_{i,j} k(f(x_i), f(G(z_j))) + \frac{1}{N^2} \sum_{i,j} k(f(G(z_i)), f(G(z_j))) \quad (17)$$

In this equation, N is the number of images, x_i is the i -th real image, z_i is the i -th random noise vector, G is the generator, $f(\cdot)$ is the feature extraction function, and $k(\cdot, \cdot)$ is a kernel function.

5) WASSERSTEIN DISTANCE (WD)

WD measures the distance between two probability distributions by calculating the optimal transport cost. Lower WD values indicate closer distribution alignment.

$$WD(P_r, P_g) = \sup_{\|f\|_L \leq 1} \mathbb{E}_{x \sim P_r} [f(x)] - \mathbb{E}_{x \sim P_g} [f(x)] \quad (18)$$

Here, P_r is the real distribution, P_g is the generated distribution, and f is a Lipschitz-1 function.

The comparative analysis of each GAN evaluation matrices among proposed RWP-GAN and existing GAN networks are given in Table 3.

For experimental purposes, we have used the Extended ALL-IDB dataset, which was originally developed by [32] and updated by [32]. To my knowledge, currently, this is the only blood cell dataset that is publicly available for RBC, WBC, and platelet analysis.

A comparative result for the proposed GAN and previously developed GAN is summarized in Table 3. This shows that the proposed model outperforms as compared to the previously developed GAN models with respect to Fréchet Inception Distance (FID), inception Score (IS), Perceptual Similarity Index (PSI), Kernel Inception Distance (KID), and Wasserstein Distance (WD). With respect to the architectural point of view, we have updated the GAN model with spectral

TABLE 4. Comparison of proposed RWP-GAN with existing GANs’ flavors.

Model Name	Pix2Pix	CycleGAN	StarGAN	DiscoGAN	DualGAN	RWPGAN
Generator Architecture	U-Net	ResNet-based	Multi-Generator	ResNet-based	U-Net	U-Net
Discriminator Architecture	PatchGAN	PatchGAN	Multi-Discriminator	PatchGAN	PatchGAN	CNN
Objective Function	L1 or L2 loss + Adversarial loss	Adversarial loss + Cycle consistency loss	Adversarial loss + Classification loss + Reconstruction loss	Adversarial loss + Reconstruction loss	Adversarial loss + Cycle consistency loss	L1 Loss + Generator loss + Discriminator loss + Generator Total Loss
Dataset Used	Cityscapes, facades, maps, edges2shoes	Various datasets without paired data	CelebA, RaFD, CUHK Face Sketch	Various datasets without paired data Various	datasets without paired data	Extended ALL-IDB 1 , Extended ALL-IDB 1
Generator Loss	L1 or L2 loss	L1 loss	L1 loss	L1 loss	L1 loss	L1 loss (MAE)
Discriminator Loss	Binary cross-entropy loss	Binary cross-entropy loss	Categorical cross-entropy loss	Binary cross-entropy loss	Binary cross-entropy loss	Binary cross-entropy loss
Pixel-wise Accuracy	High	Moderate	High	Low	Moderate	High
SSIM	High	Moderate	High	Low	Moderate	High
PSNR	High	Moderate	High	Low	Moderate	Moderate
Mean Squared Error (MSE)	High	Low	High	Low	Moderate	Low
Mean Absolute Error (MAE)	Low	Low	Moderate	Moderate	Moderate	Low
Number of Parameters	43M	11M	28M	30M	35M	57M
Contributions	adversarial loss in image-to-image translation	cycle consistency loss	multi-generator and multi-discriminator architecture	reconstruction loss	dual learning scheme	structured context-aware loss
Limitations	Requires paired data	relatively simple transformations	relatively simple transformations	relatively simple transformations	relatively simple transformations	Requires paired data

normalization and gradient penalty for segmentation based on predefined conditions. In RWP-GAN, instead of dealing with each pixel independently conditionally from all other pixels, it considers a larger receptive field and learns a structured context-aware loss. The RWP-GAN learns a mapping relation for blood cell segmentation that can compare blood cell images to their target segmented image. For the training of the proposed model with paired data for segmentation, the objective of RWP-GAN is to reduce per pixel loss L_1 as well as an adversarial loss $L_{RWP-GAN}$ to criticize the segmentation errors and joint configuration of pixels. In RWP-GAN, the adversarial loss is similar to cycle GAN loss [27], in which the Discriminator and Generator play a min-max game to minimize the errors and maximize the objective.

The authentication process of the proposed RWP-GAN is more transparent because we have performed a two-level GAN evaluation. Two-level GAN evaluation means that we initially measured each metric individually for each element of blood cells and then calculated each measure’s value globally by taking the average. The table shows that the RWP-GAN model has a lower FID score and higher IS

score than all other models except for StyleGAN2-ADA and Imagen network. But, the PSI score for the RWP-GAN model is lower than the PSI score for StyleGAN2-ADA and Imagen. The proposed model also outperforms with respect to the KID and WD. Overall, the results show that the RWP-GAN model is a promising GAN model that can generate images that are more similar to real images than other GAN models. However, there is still room for improvement in the perceptual similarity of the generated images.

F. CLASSIFICATION OF WBCCS

For the classification task on blood cell images, we utilized transfer learning with pre-trained ResNet-50, ResNet-101, and Mobile-Net models. Firstly, we get fine-tuned models on a large-scale dataset (e.g., ImageNet) to extract relevant features that can be generalized across different tasks. Then, we froze the pre-trained layers of these models and trained the remaining layers on our blood cell image dataset, namely E-ALL-IDB-I and E-ALL-IDB-II, separately.

The E-ALL-IDB-I dataset consists of two classes, namely Normal and Abnormal, while the E-ALL-IDB-II dataset

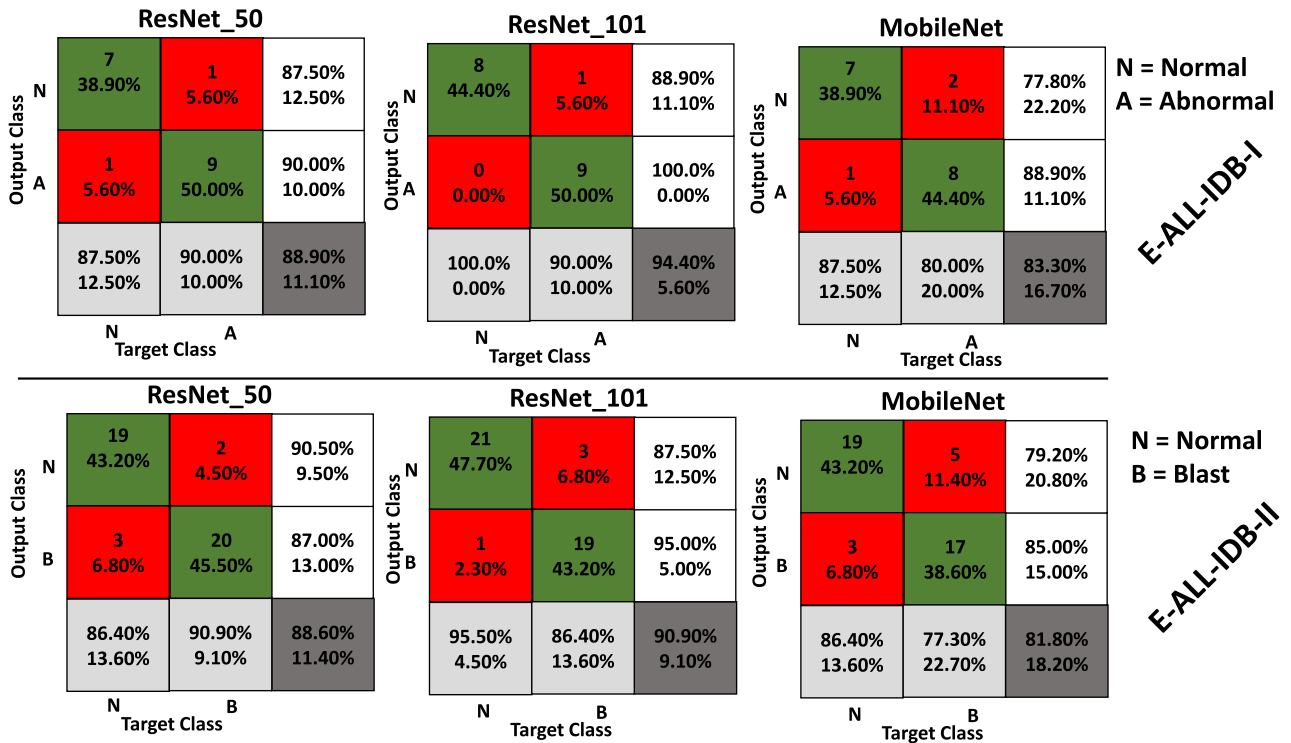


FIGURE 10. Confusion matrix: The confusion matrix for WBCs classification in both databases, E-ALL-IDB-I and E-ALL-IDB-II, is shown in the diagram. The X-axis displays the true label, while the Y-axis displays the predicted labels for WBC classification.

includes two classes, namely Normal and Blast cell. During the training process, we fed the images into the model, and the output was a predicted class label for each image.

By utilizing transfer learning, we could effectively leverage the knowledge learned from the pre-trained models and apply it to our blood cell image classification task, resulting in better accuracy and performance.

After the segmentation of WBCs and RBCs, the proposed framework classifies the WBCs of both the databases, that is, E-ALL-IDB-I and E-ALL-IDB-II into healthy or blast cells. ResNet has been used for classification in our framework because it accelerates the training speed. Residual block of ResNet avoids widening the network. ResNet adds fewer extra parameters by increasing the depth which results in faster training and higher accuracy. The residual block of ResNet minimizes the effect of vanishing gradient in deep neural networks. MobileNet has also been used for classification as it has low-latency, small size, and relatively less number of parameters. The classification performance of MobileNet is good on small, portable, and smart devices.

For classification purpose, the proposed framework uses transfer learning technique. Results reveal that the classification accuracy for E-All-IDB-I using ResNet50, ResNet101, and MobileNet is 88.88%, 94.44% and 83.33%, respectively on a 80:20 ratio for train and test images. While in case of E-All-IDB-II using ResNet50, ResNet101, and MobileNet, the classification accuracy is 88.64%, 90.91%, and 81.82%, respectively. Figure 10 depicts the WBCs classification results in the form of a confusion matrix.

V. CONCLUSION

In this paper, we have proposed novel contributions in blood cell image analysis domain. We have proposed a framework for blood cell segmentation and classification using generative adversarial networks (GANs). The proposed framework comprises of three heterogeneous GAN networks, one each for WBCs, RBCs and PLTs. All GANs work simultaneously on different patches of input image to extract the region of interest. We have also introduced E-ALL-IDB-I and ALL-IDB-II databases that comprise of manually generated mask-based blood cell database used for the authentication of segmentation and classification results. Morphological analysis is performed a using single RWP-GAN model. The proposed model increases efficiency and reduces computational time. The proposed framework gives cutting edge performance as demonstrated by the accuracy of predicted segmentation and classification results with ground truth. During training, the proposed model reduces the Generator total loss by 12.18%, 5.39%, and 3.62% for RBCs, WBCs, and PLTs, respectively. The proposed framework results in the highest pixel correctly classified (PCC) ratio for segmentation, that is, 99.8%, 93.4%, and 99.9% for WBCs, RBCs, and PLTs, respectively. Furthermore, the proposed framework attains 95.45% and 88.89% classification accuracy for WBCs for E-ALL-IDB-I and E-ALL-IDB-II datasets, respectively. In future work, we plan to enhance the RWP-GAN model for more generic medical image segmentation and classification tasks. We will explore the use of transfer learning and fine-tuning techniques

to improve the model's performance on different datasets. Additionally, we aim to investigate the potential of our model in the segmentation and classification of histopathology images, which present unique challenges due to their complex structures and variations. Finally, we will make our codes and databases publicly available for other researchers to replicate and build upon our work.

VI. CONTRIBUTIONS

Conceptualization: Zakir Khan and Muhammad Shahzad; methodology: Zakir Khan; validation: Syed Hamad Shirazi, Arslan Munir, and Yong Xie; formal analysis: Assad Rasheed and Sara Gull; investigation: Arslan Munir and Zakir Khan; resources: Syed Hamad Shirazi and Yong Xie; data curation: Muhammad Shahzad and Zakir Khan; writing—original draft preparation: Zakir Khan and Muhammad Shahzad; writing—review and editing: Arslan Munir and Syed Hamad Shirazi; visualization: Assad Rasheed and Muhammad Shahzad; supervision: Yong Xie; and project administration: Arslan Munir and Syed Hamad Shirazi.

ACKNOWLEDGMENT

The authors would like to thank Shaukat Khanum Hospital, Lahore, Pakistan, for their invaluable contribution in providing the assistance regarding annotation of the dataset for research. The assistance provided by Shaukat Khanum Hospital has been instrumental in enabling the analysis and findings presented in this study.

REFERENCES

- R. B. Hegde, K. Prasad, H. Hebbar, and B. M. K. Singh, "Development of a robust algorithm for detection of nuclei and classification of white blood cells in peripheral blood smear images," *J. Med. Syst.*, vol. 42, no. 6, pp. 1–8, Jun. 2018.
- R. B. Hegde, K. Prasad, H. Hebbar, and B. M. K. Singh, "Development of a robust algorithm for detection of nuclei of white blood cells in peripheral blood smear images," *Multimedia Tools Appl.*, vol. 78, no. 13, pp. 17879–17898, Jul. 2019.
- H. T. Madhloom, S. A. Kareem, H. Ariffin, A. A. Zaidan, H. O. Alanazi, and B. B. Zaidan, "An automated white blood cell nucleus localization and segmentation using image arithmetic and automatic threshold," *J. Appl. Sci.*, vol. 10, no. 11, pp. 959–966, May 2010.
- M. Shahzad, A. I. Umar, M. A. Khan, S. H. Shirazi, Z. Khan, and W. Yousaf, "Robust method for semantic segmentation of whole-slide digital cell microscopic images," *Comput. Math. Methods Med.*, vol. 2020, pp. 1–13, Jan. 2020.
- F. Garcia-Lamont, M. Alvarado, and J. Cervantes, "Systematic segmentation method based on PCA of image hue features for white blood cell counting," *PLoS ONE*, vol. 16, no. 12, Dec. 2021, Art. no. e0261857.
- T. F. Mahdi, H. G. Daway, and J. Jouda, "Automatic white blood cell detection depending on color features based on red and (A) in the LAB space," in *Pervasive Computing and Social Networking*. Berlin, Germany: Springer, 2022, pp. 579–588.
- T. G. Devi, N. Patil, S. Rai, and C. S. Philipose, "Gaussian blurring technique for detecting and classifying acute lymphoblastic leukemia cancer cells from microscopic biopsy images," *Life*, vol. 13, no. 2, p. 348, Jan. 2023.
- V. G. Nikitaev, O. V. Nagornov, A. N. Pronichev, E. V. Polyakov, S. M. Zaytsev, Y. V. Zakharenko, and V. V. Dmitrieva, "Research of the leukocytes segmentation method in the blood cells recognition systems," *KnE Energy*, vol. 3, no. 2, pp. 350–354, Apr. 2018.
- H. Miao and C. Xiao, "Simultaneous segmentation of leukocyte and erythrocyte in microscopic images using a marker-controlled watershed algorithm," *Comput. Math. Methods Med.*, vol. 2018, pp. 1–9, Jan. 2018.
- S. H. Shirazi, A. I. Umar, S. Naz, N. Haq, and M. I. Razzak, "Efficient enhancement and segmentation of leukocytes from microscopic images," *J. Appl. Environ. Biol. Sci.*, vol. 6, no. 35, pp. 121–126, 2016.
- M. Sajjad, S. Khan, Z. Jan, K. Muhammad, H. Moon, J. T. Kwak, S. Rho, S. W. Baik, and I. Mehmood, "Leukocytes classification and segmentation in microscopic blood smear: A resource-aware healthcare service in smart cities," *IEEE Access*, vol. 5, pp. 3475–3489, 2017.
- T. J. S. Durant, E. M. Olson, W. L. Schulz, and R. Torres, "Very deep convolutional neural networks for morphologic classification of erythrocytes," *Clin. Chem.*, vol. 63, no. 12, pp. 1847–1855, Dec. 2017.
- M. Xu, D. P. Papageorgiou, S. Z. Abidi, M. Dao, H. Zhao, and G. E. Karniadakis, "A deep convolutional neural network for classification of red blood cells in sickle cell anemia," *PLOS Comput. Biol.*, vol. 13, no. 10, Oct. 2017, Art. no. e1005746.
- Z. Tian, T. He, C. Shen, and Y. Yan, "Decoders matter for semantic segmentation: Data-dependent decoding enables flexible feature aggregation," in *Proc. IEEE/CVF Conf. Comput. Vis. Pattern Recognit. (CVPR)*, Jun. 2019, pp. 3121–3130.
- W. Sun and R. Wang, "Fully convolutional networks for semantic segmentation of very high resolution remotely sensed images combined with DSM," *IEEE Geosci. Remote Sens. Lett.*, vol. 15, no. 3, pp. 474–478, Mar. 2018.
- M. Shahzad, A. I. Umar, S. H. Shirazi, Z. Khan, A. Khan, M. Assam, A. Mohamed, and E.-A. Attia, "Identification of anemia and its severity level in a peripheral blood smear using 3-tier deep neural network," *Appl. Sci.*, vol. 12, no. 10, p. 5030, May 2022.
- M. Zhang, X. Li, M. Xu, and Q. Li, "Automated semantic segmentation of red blood cells for sickle cell disease," *IEEE J. Biomed. Health Informat.*, vol. 24, no. 11, pp. 3095–3102, Nov. 2020.
- F. Yi, I. Moon, and B. Javidi, "Cell morphology-based classification of red blood cells using holographic imaging informatics," *Biomed. Opt. Exp.*, vol. 7, no. 6, pp. 2385–2399, 2016.
- I. Goodfellow, J. Pouget-Abadie, M. Mirza, B. Xu, D. Warde-Farley, S. Ozair, A. C. Courville, and Y. Bengio, "Generative adversarial networks," *Commun. ACM*, vol. 63, no. 11, pp. 139–144, 2020.
- Y. Wang, B. Yu, L. Wang, C. Zu, D. S. Lalush, W. Lin, X. Wu, J. Zhou, D. Shen, and L. Zhou, "3D conditional generative adversarial networks for high-quality PET image estimation at low dose," *NeuroImage*, vol. 174, pp. 550–562, Jul. 2018.
- T. M. Quan, T. Nguyen-Duc, and W.-K. Jeong, "Compressed sensing MRI reconstruction using a generative adversarial network with a cyclic loss," *IEEE Trans. Med. Imag.*, vol. 37, no. 6, pp. 1488–1497, Jun. 2018.
- Q. Dou, C. Ouyang, C. Chen, H. Chen, and P.-A. Heng, "Unsupervised cross-modality domain adaptation of ConvNets for biomedical image segmentations with adversarial loss," 2018, *arXiv:1804.10916*.
- A. Negi, A. N. J. Raj, R. Nersissov, Z. Zhuang, and M. Murugappan, "RDA-UNET-WGAN: An accurate breast ultrasound lesion segmentation using Wasserstein generative adversarial networks," *Arabian J. Sci. Eng.*, vol. 45, no. 8, pp. 6399–6410, Aug. 2020.
- M. Shahzad, A. I. Umar, S. H. Shirazi, and I. A. Shaikh, "Semantic segmentation of anaemic RBCs using multilevel deep convolutional encoder-decoder network," *IEEE Access*, vol. 9, pp. 161326–161341, 2021.
- V. Alex, K. P. S. Mohammed, S. S. Chennamsetty, and G. Krishnamurthi, "Generative adversarial networks for brain lesion detection," *Proc. SPIE*, vol. 10133, pp. 113–121, Feb. 2017.
- K. Naidoo and V. Marivate, "Unsupervised anomaly detection of healthcare providers using generative adversarial networks," in *Proc. Conf. e-Business, e-Services e-Society*. Springer, 2020, pp. 419–430.
- J.-Y. Zhu, T. Park, P. Isola, and A. A. Efros, "Unpaired image-to-image translation using cycle-consistent adversarial networks," in *Proc. IEEE Int. Conf. Comput. Vis. (ICCV)*, Oct. 2017, pp. 2242–2251.
- G. E. Hinton, N. Srivastava, A. Krizhevsky, I. Sutskever, and R. R. Salakhutdinov, "Improving neural networks by preventing co-adaptation of feature detectors," 2012, *arXiv:1207.0580*.
- P. Isola, J.-Y. Zhu, T. Zhou, and A. A. Efros, "Image-to-image translation with conditional adversarial networks," in *Proc. IEEE Conf. Comput. Vis. Pattern Recognit. (CVPR)*, Jul. 2017, pp. 5967–5976.
- O. Ronneberger, P. Fischer, and T. Brox, "U-Net: Convolutional networks for biomedical image segmentation," in *Proc. Int. Conf. Med. Image Comput. Comput.-Assist. Intervent*. Springer, 2015, pp. 234–241.
- M. Mirza and S. Osindero, "Conditional generative adversarial nets," 2014, *arXiv:1411.1784*.

- [32] R. D. Labati, V. Piuri, and F. Scotti, "All-IDB: The acute lymphoblastic leukemia image database for image processing," in *Proc. 18th IEEE Int. Conf. Image Process.*, Sep. 2011, pp. 2045–2048.
- [33] D. P. Kingma and J. Ba, "Adam: A method for stochastic optimization," 2014, *arXiv:1412.6980*.
- [34] M. H. Mozaffari, P. Abolghader, L.-L. Tay, and A. Stolow, "Segmentation of stimulated Raman microscopy images using a 1D convolutional neural network," in *Proc. Photon. North (PN)*, May 2022.
- [35] X. Chen, Y. Duan, R. Houthoofd, J. Schulman, I. Sutskever, and P. Abbeel, "InfoGAN: Interpretable representation learning by information maximizing generative adversarial nets," 2016, *arXiv:1606.03657*.
- [36] T. Salimans, I. Goodfellow, W. Zaremba, V. Cheung, A. Radford, and X. Chen, "Improved techniques for training GANs," 2016, *arXiv:1606.03498*.
- [37] Y. Li, C. Zhang, and X. Zhang, "A Liouville theorem on complete non-Kähler manifolds," 2018, *arXiv:1805.11215*.
- [38] X. Huang, M.-Y. Liu, S. Belongie, and J. Kautz, "Multimodal unsupervised image-to-image translation," 2018, *arXiv:1804.04732*.
- [39] A. van den Oord, Y. Li, and O. Vinyals, "Representation learning with contrastive predictive coding," 2018, *arXiv:1807.03748*.
- [40] T. Karras, "StyleGAN2: An improved generative adversarial network for fewer parameters and higher quality images," *IEEE Trans. Image Process.*, vol. 29, pp. 2049–2067, 2020.
- [41] C. Peng, Y. S. Kim, and S. Mittnik, "Portfolio optimization on multivariate regime switching GARCH model with normal tempered stable innovation," 2020, *arXiv:2009.11367*.
- [42] S. Richard and N. Tszu, "Spectral and scattering theory for topological crystals perturbed by infinitely many new edges," 2021, *arXiv:2107.08541*.
- [43] J. Lu and S. Meyer, "A zero-inflated endemic-epidemic model with an application to measles time series in Germany," 2022, *arXiv:2201.07285*.
- [44] A. Iqbal, M. Sharif, M. Yasmin, M. Raza, and S. Aftab, "Generative adversarial networks and its applications in the biomedical image segmentation: A comprehensive survey," *Int. J. Multimedia Inf. Retr.*, vol. 11, no. 3, pp. 333–368, Sep. 2022, doi: [10.1007/s13735-022-00240-x](https://doi.org/10.1007/s13735-022-00240-x).
- [45] A. Iqbal and M. Sharif, "PDF-UNet: A semi-supervised method for segmentation of breast tumor images using a U-shaped pyramid-dilated network," *Exp. Syst. Appl.*, vol. 221, Jul. 2023, Art. no. 119718, doi: [10.1016/j.eswa.2023.119718](https://doi.org/10.1016/j.eswa.2023.119718).
- [46] K. Barrera, J. Rodellar, S. Alférez, and A. Merino, "Automatic normalized digital color staining in the recognition of abnormal blood cells using generative adversarial networks," *Comput. Methods Programs Biomed.*, vol. 240, Oct. 2023, Art. no. 107629, doi: [10.1016/j.cmpb.2023.107629](https://doi.org/10.1016/j.cmpb.2023.107629).
- [47] K. Barrera, A. Merino, A. Molina, and J. Rodellar, "Automatic generation of artificial images of leukocytes and leukemic cells using generative adversarial networks (syntheticcellgan)," *Comput. Methods Programs Biomed.*, vol. 229, Feb. 2023, Art. no. 107314, doi: [10.1016/j.cmpb.2022.107314](https://doi.org/10.1016/j.cmpb.2022.107314).
- [48] D. Hazra, Y.-C. Byun, and W. J. Kim, "Enhancing classification of cells procured from bone marrow aspirate smears using generative adversarial networks and sequential convolutional neural network," *Comput. Methods Programs Biomed.*, vol. 224, Sep. 2022, Art. no. 107019, doi: [10.1016/j.cmpb.2022.107019](https://doi.org/10.1016/j.cmpb.2022.107019).
- [49] M. I. Cosacak and C. Kizil, "Using conditional generative adversarial networks (GAN) to generate de novo synthetic cell nuclei for training machine learning-based image segmentation," Tech. Rep., 2022, doi: [10.1101/2022.11.12.516283](https://doi.org/10.1101/2022.11.12.516283).
- [50] S. Xun, D. Li, H. Zhu, M. Chen, J. Wang, J. Li, M. Chen, B. Wu, H. Zhang, and X. Chai, "Generative adversarial networks in medical image segmentation: A review," *Comput. Biol. Med.*, vol. 140, Jan. 2022, Art. no. 105063.
- [51] A. Makhlof, M. Maayah, N. Abughanam, and C. Catal, "The use of generative adversarial networks in medical image augmentation," *Neural Comput. Appl.*, vol. 35, no. 34, pp. 24055–24068, 2023.
- [52] O. N. Oyelade and A. E. Ezugwu, "A novel wavelet decomposition and transformation convolutional neural network with data augmentation for breast cancer detection using digital mammogram," *Sci. Rep.*, vol. 12, no. 1, p. 5913, Apr. 2022.
- [53] L. I. Song, K. F. Geoffrey, and H. E. Kaijian, "Bottleneck feature supervised U-Net for pixel-wise liver and tumor segmentation," *Exp. Syst. Appl.*, vol. 145, May 2020, Art. no. 113131.
- [54] L. Ma, R. Shuai, X. Ran, W. Liu, and C. Ye, "Combining DC-GAN with ResNet for blood cell image classification," *Med. Biol. Eng. Comput.*, vol. 58, pp. 1251–1264, Jun. 2020.
- [55] M. M. A. Jamil, L. Oussama, W. M. Hafizah, M. H. A. Wahab, and M. F. Johan, "Computational automated system for red blood cell detection and segmentation," in *Intelligent Data Analysis for Biomedical Applications*, 2019, pp. 173–189.
- [56] A. Gorey, D. Biswas, A. Kumari, S. Gupta, N. Sharma, G. C. K. Chen, and S. Vasudevan, "Application of continuous-wave photoacoustic sensing to red blood cell morphology," *Lasers Med. Sci.*, vol. 34, pp. 487–494, Apr. 2019.
- [57] S. Mishra, B. Majhi, P. K. Sa, and L. Sharma, "Gray level co-occurrence matrix and random forest based acute lymphoblastic leukemia detection," *Biomed. Signal Process. Control*, vol. 33, pp. 272–280, Mar. 2017.
- [58] H. Abedy, F. Ahmed, M. N. Q. Bhuiyan, M. Islam, N. Y. Ali, and M. Shamsujjoha, "Leukemia prediction from microscopic images of human blood cell using HOG feature descriptor and logistic regression," in *Proc. 16th Int. Conf. ICT Knowl. Eng.*, Nov. 2018, pp. 1–6.
- [59] A. Molina, S. Alférez, L. Boldu, A. Acevedo, J. Rodellar, and A. Merino, "Sequential classification system for recognition of malaria infection using peripheral blood cell images," *J. Clin. Pathol.*, vol. 73, no. 10, pp. 665–670, Oct. 2020.
- [60] J. M. Patel and N. C. Gamit, "A review on feature extraction techniques in content based image retrieval," in *Proc. Int. Conf. Wireless Commun., Signal Process. Netw. (WiSPNET)*, Mar. 2016, pp. 2259–2263.
- [61] V. Wasson, "An efficient content based image retrieval based on speeded up robust features (SURF) with optimization technique," in *Proc. 2nd IEEE Int. Conf. Recent Trends Electron., Inf. Commun. Technol. (RTEICT)*, May 2017, pp. 730–735.
- [62] Y. Li, Q. Li, Y. Liu, and W. Xie, "A spatial-spectral SIFT for hyperspectral image matching and classification," *Pattern Recognit. Lett.*, vol. 127, pp. 18–26, Nov. 2019.
- [63] S. Li, Z. Wang, and Q. Zhu, "A research of ORB feature matching algorithm based on fusion descriptor," in *Proc. IEEE 5th Inf. Technol. Mechatronics Eng. Conf. (ITOEC)*, Jun. 2020, pp. 417–420.
- [64] M. Agrawal, K. Konolige, and M. R. Blas, "CenSurE: Center surround extremas for realtime feature detection and matching," in *Proc. Eur. Conf. Comput. Vis.* Springer, 2008, pp. 102–115.
- [65] J. Ma, X. Jiang, A. Fan, J. Jiang, and J. Yan, "Image matching from handcrafted to deep features: A survey," *Int. J. Comput. Vis.*, vol. 129, no. 1, pp. 23–79, Jan. 2021.
- [66] R. Anand, T. Shanthi, M. S. Nithish, and S. Lakshman, "Face recognition and classification using GoogleNET architecture," in *Soft Computing for Problem Solving*, vol. 1. Berlin, Germany: Springer, 2020, pp. 261–269.
- [67] A. Khan, A. Khan, M. Ullah, M. M. Alam, J. I. Bangash, and M. M. Suud, "A computational classification method of breast cancer images using the VGGNet model," *Frontiers Comput. Neurosci.*, vol. 16, Nov. 2022, Art. no. 1001803.
- [68] S. Saleem, J. Amin, M. Sharif, M. A. Anjum, M. Iqbal, and S. H. Wang, "A deep network designed for segmentation and classification of leukemia using fusion of the transfer learning models," *Complex Intell. Syst.*, pp. 1–16, Jul. 2021.



ZAKIR KHAN received the M.S. degree in computer science from Hazara University Mansehra, Mansehra, Pakistan. He is currently pursuing the Ph.D. degree in computer science. He is also a Lecturer in computer science with Hazara University Mansehra. His skills and expertise are computer vision, texture analysis, neural networks, object recognition, pattern recognition, digital image processing, and machine learning and wavelet transformation.



SYED HAMAD SHIRAZI received the M.S. degree in computer science from COMSATS Abbottabad, Pakistan, and the Ph.D. degree from the Department of Information Technology, Hazara University Mansehra, Pakistan. He is currently an Assistant Professor with the Department of Computer Science and Information Technology. His skills and expertise are computer vision, texture analysis, neural networks, object recognition, pattern recognition, digital image processing, and machine learning and wavelet transformation.



ASSAD RASHEED received the M.S. degree in computer science from Hazara University Mansehra, Pakistan. He is currently an Assistant Director (Information Technology) with the Establishment Department, Government of Khyber Pakhtunkhwa. He is also a Ph.D. Scholar with the Department of Computer Science and Information Technology, Hazara University Mansehra. His research interests include artificial intelligence, machine learning, deep learning, pattern recognition, natural language processing, and medical imaging.



MUHAMMAD SHAHZAD received the M.S. degree in computer science from the Virtual University of Pakistan. He is currently a Ph.D. Scholar with the Department of Information Technology, Hazara University Manshera, Pakistan. His research interests include data mining, machine learning, deep learning, medical image processing, and bioinformatics.



YONG XIE received the Ph.D. degree in computer science from Wuhan University, Wuhan, China, in 2016. He is currently an Associate Professor with the Department of Computer Technology and Application, Qinghai University. His current research interests include next-generation internet, network protocol, and protocol security.



ARSLAN MUNIR (Senior Member, IEEE) is currently an Associate Professor with the Department of Computer Science (CS), Kansas State University (K-State). He is also an affiliated (ancillary) Faculty Member of the Department of Electrical and Computer Engineering, K-State. He joined K-State as a tenure-track Assistant Professor, in June 2017. Before joining K-State, he was a tenure-track Assistant Professor with the Department of Computer Science and Engineering (CSE), University of Nevada, Reno (UNR), from July 2014 to June 2017. He was a Postdoctoral Research Associate with the Electrical and Computer Engineering (ECE) Department, Rice University, Houston, TX, USA, from May 2012 to June 2014. His current research interests include embedded and cyber-physical systems, secure and trustworthy systems, computer architecture, artificial intelligence (AI), computer vision, parallel computing, and fault tolerance.

SARAH GUL received the Ph.D. degree in molecular medicine from Ulm University, Germany, in 2014. She has been an Assistant Professor with the Department of Biological Sciences, Islamic International University Islamabad, Pakistan, since 2015. Her area of research expertise are molecular medicine, cancer genetics, molecular biology, advanced microbiology, biomedical image processing, pollution detectors, genetic manipulation, metabolic engineering, nanoparticles as antibacterial/antifungal/antioxidant agents, food biotechnology, type 2 diabetic and over activation of transcription factors in mice models, and application of AI for solutions for biological problems.

...